NTNU

Norwegian University of
Science and Technology

Properties of gold clusters and molecule-coated gold clusters as studied by molecular modeling

Martin E Walderhaug

Preface

A number of people deserve thanks for contributions to this thesis.

My supervisor, Per-Olof Åstrand, for all his helpful guidance and advice.

My co-supervisor, Fernando Bresme, for useful discussions on the direction of the project.

Mehdi Mahmoodinia, for assisting me with the use of ADF.

<div align="right">

Martin E. Walderhaug

Trondheim, June 2016

</div>

Abstract

The properties of small gold clusters are studied by use of density functional theory (DFT). A method validation study is conducted to choose a suitable DFT method. Geometry optimizations are performed on a number of different clusters, and their cohesive energies are computed. The charge distribution in the Au_{20} cluster is studied, both in the presence and absence of an electric field. The results are interpreted in terms of a model for the atomic charges in the cluster derived from electronegativity equalization. The interaction between Au_{20} and CO is studied, considering different possible adsorption sites on the face of the cluster. Only certain sites are found to give favourable interaction between the two subsystems.

2

Sammendrag

Egenskapene til små gullklynger studeres ved bruk av tetthetsfunksjonalteori (DFT). En valideringsstudie gjennomføres for å velge en egnet DFT-metode. Geometrioptimeringer gjennomføres for et utvalg klynger, og bindingsenergi per atom for klyngene beregnes. Ladningsfordelingen i en Au_{20}-klynge studeres, både med og uten tilstedeværelse av et homogent eksternt elektrisk felt. Resultatene tolkes ut fra en modell for atomladningene utledet fra elektronegativitetsutligning. Interaksjonen mellom Au_{20} og CO studeres. Mulige adsorpsjonspunkter på klyngeoverflaten vurderes. Kun enkelte punkter gir gunstig interaksjon mellom de to subsystemene.

Contents

1 Introduction

Gold, being an inert metal in its bulk form, has traditionally not been regarded as the most interesting of elements from a chemical perspective [1]. However, during the last decades research interest has increased tremendously after the discovery of novel properties for gold structures of smaller dimensions. Gold was observed to be highly active as a catalyst in a number of reactions [2, 3], for instance oxidation of CO, and the field of gold catalysis is now a vibrant scene of new discovery.

With new experimental discoveries come a desire to understand the theoretical foundations of the observed phenomena. Hence, there has been a substantial amount of effort put in not only on the experimental side, but also to understand the theoretical chemistry of gold, with a number of reviews written on the subject [4–6]. In this context, gold clusters of a size on the order of tens of atoms have attracted a significant amount of research interest [7]. Their rich variety in structure and properties in combination with their manageable size from a computational perspective make them interesting model systems. Numerous papers have been written discussing the minimum structures of small gold clusters, spanning methodology from computer-based global minimum searches[8] to combined experimental and theoretical studies where photoelectron spectroscopy and density functional theory are used for structural elucidation [9]. Still, ambiguity remains about the structures of all but a handful of clusters.

Given the comprehensive experimental interest in gold catalysis of the oxidation of carbon monoxide, the interaction between gold and CO has also gained the interest of theoretical chemists, with several papers written on the topic [10, 11].

Density functional theory (DFT) is often employed in computational studies on gold. It could be described as the workhorse of computational chemistry in recent years. Since the landmark developments by Hohenberg, Kohn and Sham in the 1960s [12, 13], increasingly accurate approximations to the elusive exchange-correlation functional have been introduced. While the research field is still highly active, with significant improvements surely to be made in the years to come, DFT in its current state yields results of useful accuracy at a fraction of the computational cost of comparable wave-function-based methods. Its efficiency means it is in many cases the only option for computational study of gold clusters of a certain size, as wave-function based methods become prohibitively expensive in terms of computing resources.

In this work, a DFT study will be conducted in an endeavor to contribute to the understanding of the chemistry of gold clusters. A method validation study will be conducted to choose a suitable DFT method, by calculating some select structural and energetic properties of the gold dimer and tetramer. The chosen method will then be employed to

study the charge distribution in gold clusters, both in the absence and presence of a homogeneous external electric field. The interaction between CO and the Au_{20} cluster will be studied, considering different possible coordination sites on the surface of the cluster.

2 Theory

The following chapter will present the theoretical framework for density functional theory, including but not limited to the Hohenberg-Kohn theorems [12], the Kohn-Sham formalism [13], and the different classes of density functionals developed to deal with the exchange-correlation energy. An orbital localization scheme [14] used to aid result interpretation will be briefly described. Electronegativity equalization [15] will be used to derive expressions describing the charge distribution in the tetrahedral Au_{20} cluster, both in the presence and absence of an electric field.

2.1 Quantum chemistry - important concepts

2.1.1 The Schrödinger equation

Phenomena at an atomic scale are governed by quantum mechanics. Where classical mechanics gives a deterministic description of reality, the quantum picture is a statistical one. This stems from the inherently uncertain character of nature at a small scale, where there is a limit to how precisely certain combinations of variables may be known, as expressed in the Heisenberg uncertainty principle. At the heart of this physical paradigm is the so-called wave function, a mathematical construct containing complete information about the system it describes. When the wave function is known, every piece of information attainable within the limits imposed by the uncertainty principle is in principle known. While the wave function itself has no physical interpretation, its square modulus is interpreted as the probability density to find the system in a particular state. This is known as the Born interpretation. The wave function is usually found by solving the Schrödinger equation, which is central to quantum mechanics. In its time-independent form, it may be succinctly expressed as

$$\hat{H}\Psi_i = E_i\Psi_i \; , \tag{1}$$

where $\hat{H}$ is the Hamiltonian operator of the system, Ψ_i is the wave function describing the ith state of the system, and E_i is the energy corresponding to this state. Note that Ψ is a function of the coordinates of all the particles in the system, including the spin of e.g. any electrons. Equation (1) is an eigenvalue equation, that is, the set of solutions consists of all eigenvectors Ψ_i and corresponding eigenvalues E_i of the operator $\hat{H}$. In the case of a chemical system, the sheer number of particles makes finding an exact analytical solution to equation (1) impossible even for relatively small molecules. Hence, numerical solution schemes are a necessity.

2.1.2 The Born-Oppenheimer approximation

A chemical system typically consists of a number of electrons and atomic nuclei. The significant difference in mass between these two classes of particles leads to what has become a standard approximation employed in quantum chemistry, the so-called Born-Oppenheimer approximation. A nucleus has a mass several orders of magnitude greater than an electron. Even in the case of a small hydrogen nucleus, the ratio between the nuclear and electron mass is ≈ 1800. Recognizing this, in the Born-Oppenheimer approximation the electrons are regarded as moving in the field of stationary nuclei. That is, the positions of the nuclei are frozen, meaning they only enter parametrically in the Schrödinger equation. Effectively, this means the problem has been reduced to finding the electronic wave function. While still a formidable task, this makes the problem significantly more manageable.

The electronic Schrödinger equation has the familiar form of equation (1), albeit with an electronic Hamiltonian $\hat{H}_{elec}$ which may be expressed as

$$\hat{H}_{elec} = -\frac{1}{2}\sum_{i=1}^{N}\nabla_i^2 - \sum_{i=1}^{N}\sum_{A=1}^{M}\frac{Z_A}{r_{iA}} + \sum_{i=1}^{N}\sum_{j>i}^{N}\frac{1}{r_{ij}} \ , \tag{2}$$

where N and M are the number of electrons and nuclei, respectively, Z_A is the charge of nucleus A, r_{ij} is the distance between electrons i and j, and similarly r_{iA} is the distance between electron i and nucleus A. Note that atomic units have been assumed. The first term represents the kinetic energy of the electrons, while the last two terms are the potential energy of the electrostatic interaction between an electron and a nucleus or another electron, respectively. Unless stated otherwise, any further reference to the Schrödinger equation or the Hamiltonian operator in this text will be referring to the electronic problem within the Born-Oppenheimer approximation.

2.1.3 The variational principle

The variational principle constitutes a central piece of the theoretical background of many quantum chemical methods. It states that the expectation value of the Hamiltonian $\hat{H}$ computed with a trial wave function Ψ_{trial} is always greater than or equal to the ground state energy of the real physical system. Assuming Ψ_{trial} is normalized, the variational principle can be expressed mathematically as the following inequality:

$$\left\langle \Psi_{trial} \left| \hat{H} \right| \Psi_{trial} \right\rangle \geq \left\langle \Psi_0 \left| \hat{H} \right| \Psi_0 \right\rangle = E_0 \tag{3}$$

Here Ψ_0 is the ground state wave function, and E_0 the corresponding energy.

2.2 Density functional theory

While traditional wave function based methods aim to compute the wave function and obtain any properties of interest from that, density functional theory takes a different approach. By sidestepping the wave function and computing the electron density $\rho(\vec{r})$ instead, the method achieves a significant reduction in computational complexity. This is in part due to the electron density being a function of only three variables, while the wave function is a function of the coordinates of every single particle in the system.

2.2.1 The Hohenberg-Kohn theorems

The theoretical foundation of DFT rests on two important theorems published in a landmark paper by P. Hohenberg and W. Kohn in 1964 [12]. The first one states that the electronic ground state, and hence the ground state energy and any other properties of interest, is a functional of the electron density $\rho(\vec{r})$. That is,

$$E_0 = E[\rho_0(\vec{r})] \ , \tag{4}$$

where the subscript 0 on the electron density signifies the ground state density, and the $E[]$ is some unknown functional. Briefly, the proof rests on the fact that the electron density uniquely determines the external potential (i.e. the potential due to the nuclei in chemical applications). In turn, this external potential fixes the Hamiltonian, which determines the wave function and hence any property of the system. The importance of this theorem lies in the fact that it provides a solid theoretical foundation for all further developments within density functional theory, as it shows that expressing the energy of the system as a functional of the electron density is theoretically sound.

While the first Hohenberg-Kohn theorem provides theoretical justification for using the electron density as the primary quantity in a molecular electronic structure theory, the question of how to identify a correct ground state electron density for a given system still remains. A formal answer to this question is provided by the second Hohenberg-Kohn theorem, which establishes a variational principle for density functional theory. It states that

$$E_0 = E[\rho_0(\vec{r})] \leq E[\rho_{trial}(\vec{r})] \ , \tag{5}$$

where $\rho_{trial}(\vec{r})$ is a trial density. That is, the true ground state electron density is the density which minimizes the energy as given by the energy functional. Hence, a formal prescription for finding the actual ground state density describing a system is provided. Note that even though the Hohenberg-Kohn theorems are of great theoretical significance, they are of limited practical relevance. While the first theorem proves that a functional

mapping the electron density to the energy exists, it says nothing about its actual form. Likewise, regarding the second theorem, a search over all possible electron densities is of course intractable in practice. Furthermore, the second theorem presupposes that the exact functional is known, which unfortunately is not the case.

2.2.2   The Kohn-Sham formalism

The second major breakthrough in density functional theory came with a paper by W. Kohn and L. J. Sham in 1965 [13]. While the Hohenberg-Kohn theorems provide the theoretical framework for density functional theory, what has become known as the Kohn-Sham formalism provides a formulation of the theory which is actually computationally manageable.

It follows from the first Hohenberg-Kohn theorem that not only the energy, but also its individual components must be a functional of the density. Hence, within the Born-Oppenheimer approximation the energy functional may be expressed as

$$E[\rho] = T[\rho] + E_{ee}[\rho] + E_{Ne}[\rho] \tag{6}$$

where T is the electronic kinetic energy, E_{ee} is the electrostatic electron-electron interaction, and E_{Ne} is the electrostatic nucleus-electron interaction. Note that the total energy of the system also includes a term corresponding to the nucleus-nucleus electrostatic interaction. This is constant within the Born-Oppenheimer approximation, and is simply added to the energy given by equation (6) at the end of a calculation. With the exception of E_{Ne}, which may be expressed simply as

$$E_{Ne}[\rho] = \int \rho(\vec{r}) V_{Ne}(\vec{r}) d\vec{r} \tag{7}$$

where V_{Ne} is the electrostatic potential due to the nuclei, the component functionals in equation (6) are unknown. Some progress may be made by separating E_{ee} into two terms as follows:

$$E_{ee}[\rho] = J[\rho] + E_{ncl}[\rho] = \frac{1}{2} \int \int \frac{\rho(\vec{r_1})\rho(\vec{r_2})}{r_{12}} d\vec{r_1} d\vec{r_2} + E_{ncl}[\rho] \tag{8}$$

where r_{12} is the distance between points 1 and 2 in space, $J[\rho]$ is the classical electrostatic interaction between two charge distributions, and $E_{ncl}[\rho]$ contains all non-classical contributions to the electron-electron interactions in addition to a self-interaction correction. The latter is necessary to correct the unphysical inclusion of interaction energy between a particle and itself in $J[\rho]$. E.g. even a system containing only a single electron would have a non-zero $J[\rho]$. The non-classical contributions to the electron-electron interactions may be broadly categorized into two distinct parts, namely exchange and correlation ef-

fects. Exchange is a direct consequence of the Pauli exclusion principle, stating that no two electrons may be found in the same state. The qualitative consequence of this is that electrons of the same spin tend to avoid each other, resulting in a net lowering of the electrostatic repulsion. Correlation is related to the instantaneous repulsion between electrons, taking into account the fact that electrons are point particles with correlated motion rather than the static charge distribution embodied in $J[\rho]$.

While E_{ncl} constitutes a significant, but relatively small part of the total energy, a more immediate problem is presented by the unknown form of T, the kinetic energy functional. This is where Kohn and Sham made significant headway with their new formalism. The central idea is the definition of a non-interacting reference system, consisting of fictitious non-interacting electrons moving in an average potential. By construction, the electron density of the reference system should be exactly equal to the one in the real system. The Hamiltonian $\hat{H}_{KS}$ of the reference system is given by

$$\hat{H}_{KS} = -\frac{1}{2}\sum_i^N \nabla_i^2 + \sum_i^N V_{KS}(\vec{r}_i) \tag{9}$$

where the sums over i run to the total number of electrons N, and V_{KS} is an effective potential. The wave function of such a system is a Slater determinant Φ_{KS}, which can be expressed in terms of a set of one-electron spin orbitals $\chi_i(\vec{x}_j)$ (where $\vec{x}_j$ denotes dependence on the spin coordinate as well as the spatial coordinates of the relevant electron) as follows:

$$\Phi_{KS} = \frac{1}{\sqrt{N!}} \begin{vmatrix} \chi_1(\vec{x_1}) & \chi_2(\vec{x_1}) & \cdots & \chi_N(\vec{x_1}) \\ \chi_1(\vec{x_2}) & \chi_2(\vec{x_2}) & \cdots & \chi_N(\vec{x_2}) \\ \vdots & \vdots & \ddots & \vdots \\ \chi_1(\vec{x_N}) & \chi_2(\vec{x_N}) & \cdots & \chi_N(\vec{x_N}) \end{vmatrix} \tag{10}$$

The spin orbitals χ_i are determined by a set of one-electron equations of the form

$$\hat{f}_{KS}\chi_i = \epsilon_i\chi_i \ , \tag{11}$$

where ϵ_i is the eigenvalue of each orbital, and $\hat{f}_{KS}$ is a one-electron operator defined as

$$\hat{f}_{KS} = -\frac{1}{2}\nabla^2 + V_{KS}(\vec{r}). \tag{12}$$

The electron density ρ_{KS} of the reference system is given by

$$\rho_{KS}(\vec{r}) = \sum_i^N \sum_\sigma |\chi_i(\vec{r},\sigma)|^2 \ , \tag{13}$$

where the sum over σ signifies a sum over possible electron spin states. The essence of the Kohn-Sham formalism lies in defining V_{KS} such that $\rho_{KS} = \rho_0$.

Returning to equation (6) and substituting equations (7) and (8) for two of the terms, the expression becomes

$$E[\rho] = T[\rho] + \frac{1}{2} \int \int \frac{\rho(\vec{r_1})\rho(\vec{r_2})}{r_{12}} d\vec{r_1}d\vec{r_2} + E_{ncl}[\rho] + \int \rho(\vec{r})V_{Ne}(\vec{r})d\vec{r} \; . \tag{14}$$

Now, introducing the functional $T_{KS}[\rho]$, which is by definition the kinetic energy of the non-interacting system, equation (14) may be rewritten as

$$E[\rho] = T[\rho] - T_{KS}[\rho] + T_{KS}[\rho] + \frac{1}{2} \int \int \frac{\rho(\vec{r_1})\rho(\vec{r_2})}{r_{12}} d\vec{r_1}d\vec{r_2} + E_{ncl}[\rho] + \int \rho(\vec{r})V_{Ne}(\vec{r})d\vec{r} \tag{15}$$

$$= T_{KS}[\rho] + \frac{1}{2} \int \int \frac{\rho(\vec{r_1})\rho(\vec{r_2})}{r_{12}} d\vec{r_1}d\vec{r_2} + E_{XC}[\rho] + \int \rho(\vec{r})V_{Ne}(\vec{r})d\vec{r} \tag{16}$$

where the last line defines $E_{XC}[\rho]$, the exchange-correlation functional. It includes both the non-classical contributions to the electron-electron interactions, the difference between the electronic kinetic energy of the real, interacting system and that of the reference system, and a self-interaction correction. While T_{KS} as a functional of the density is unknown, in terms of orbitals it is defined simply as

$$T_{KS} = -\frac{1}{2} \sum_{i=1}^{N} \langle \chi_i | \nabla^2 | \chi_i \rangle \; . \tag{17}$$

If the density ρ in equation (16) is expressed in terms of orbitals analogously to equation (13), the resulting expression may be minimized with respect to variations in the orbitals to obtain the ground state energy and corresponding density in accordance with the variational principle (5). Minimization subject to the constraint of orthonormal orbitals results in a set of equations like equation (11), provided that $V_{KS}(\vec{r})$ is defined as follows:

$$V_{KS}(\vec{r_i}) = \int \frac{\rho(\vec{r_2})}{r_{12}} d\vec{r_2} + V_{XC}(\vec{r_i}) - \sum_{A=1}^{M} \frac{Z_A}{r_{iA}} \tag{18}$$

V_{XC} is defined as the functional derivative of E_{XC}, that is $V_{XC} = \frac{\delta E_{XC}}{\delta \rho}$. Hence, by choosing V_{KS} as given by (18), the electron density and energy of the real, interacting system may be obtained by solving the equations governing the non-interacting reference system.

2.2.3 Basis sets

In any actual implementation of the Kohn-Sham formalism, a specific representation has to be chosen for the orbitals of equation (13). In wave-function-based methods, it is customary to expand molecular orbitals in terms of atomic orbitals. That is, the actual atomic orbitals are not used, but a set of functions centered on each atom in the molecule, having a form chosen to resemble the atomic orbitals. Given the vast amount of accumulated experience with this kind of basis, taking a similar approach in Kohn-Sham DFT is advantageous. Mathematically, the expansion of molecular orbitals as a linear combination of atomic orbitals can be expressed as

$$\chi_i = \sum_{\alpha=1}^{L} c_{i\alpha} \eta_\alpha \tag{19}$$

where η_α is a basis function, $c_{i\alpha}$ is a constant to be determined, and L is the number of basis functions. The basis functions are kept constant throughout the minimization procedure, hence the coefficients of the linear combination are what is varied. A possible choice of function type for η is so-called Slater type orbitals. This is the choice made in the ADF software [16].

A practical aspect of the expansion in atomic orbitals is that the set of basis functions has to be finite in real-world applications, while exact representation of any molecular orbital would require an infinite set. This introduces an error in the calculation as a consequence of the incomplete nature of the basis set employed, with the resulting imperfect description of the exact Kohn-Sham orbitals. A specific manifestation of this is the so-called basis set superposition error (BSSE). This term describes an unphysical lowering of the binding energy between two subsystems, because each subsystem is described by an incomplete basis and therefore benefits from the additional basis functions introduced by the other subsystem. This effect is often corrected for in calculations, for instance by use of the so-called counterpoise correction [17]. This involves calculating the energy of each subsystem in the basis used for the complete system, hence eliminating the difference in basis set completeness.

Computationally, the consequence of introducing a set of fixed basis functions is that the set of equations like equation (11) is reduced to a linear algebra problem, namely solving the following equation:

$$\mathbf{F}^{KS}\mathbf{C} = \mathbf{S}\mathbf{C}\boldsymbol{\epsilon} \ . \tag{20}$$

The matrix $\mathbf{F}_{KS}$ is defined by $F_{\mu\nu}^{KS} = \langle \eta_\mu | \hat{f}_{KS} | \eta_\nu \rangle$, the elements of $\mathbf{C}$ are the coefficients $c_{i\alpha}$, the overlap matrix $\mathbf{S}$ is defined by $S_{\mu\nu} = \langle \eta_\mu | \eta_\nu \rangle$, and $\boldsymbol{\epsilon}$ is a diagonal matrix of the eigenvalues ϵ_i from equation (11). Equation (20) is solved through the iterative *self-*

consistent field (SCF) procedure, as the operator $\hat{f}_{KS}$ depends on the very orbitals one attempts to find by solving the equation.

2.2.4 The exchange-correlation functional

The Kohn-Sham formalism is in principle exact. However, as the form of the exchange-correlation functional $E_{XC}[\rho]$ is unknown, approximations to this unknown term have to be used in practical applications. This is an area of active research, and efforts are constantly being put in to develop ever better exchange-correlation functionals. An early attempt was the so-called *local density approximation* (LDA). The exchange-correlation energy is assumed to depend only on the electron density (and not its derivatives):

$$E_{XC}^{LDA}[\rho] = \int f(\rho)d\vec{r} \tag{21}$$

The LDA proved to be too simple for chemical applications. The *generalized gradient approximation* (GGA), however, has enjoyed a significant amount of success. It improves on the LDA by also taking the gradient of the electron density into account:

$$E_{XC}^{GGA}[\rho] = \int f(\rho, \nabla\rho)d\vec{r} \tag{22}$$

Examples of GGA-functionals include the popular PBE functional introduced by Perdew, Burke and Ernzerhof [18]. Further improvement on the GGA was attempted by the introduction of the *meta-generalized gradient approximation* (meta-GGA). Meta-GGA-functionals take the second order derivatives of the density into account:

$$E_{XC}^{mGGA}[\rho] = \int f(\rho, \nabla\rho, \nabla^2\rho)d\vec{r} \tag{23}$$

Examples of meta-GGA-functionals include TPSS [19, 20] and M06-L [21, 22].

An additional trend in the development of exchange-correlation functionals is the inclusion of a component of Hartree-Fock exchange, leading to so-called *hybrid* functionals. This is motivated by the exact treatment of the exchange interactions in Hartree-Fock theory. Several popular functionals are hybrids, notably the popular B3LYP-functional [23].

2.2.5 Dispersion correction

DFT-D3(BJ)[24] is one in a series of approaches developed by Grimme and others to remedy the bad performance of density functional theory on systems involving significant nonbonded interactions. It involves adding an energy term resembling a potential from

molecular mechanics to account for London dispersion effects. More precisely, the introduced potential is pairwise additive, and the dispersion energy $E_{disp}^{D3(BJ)}$ may be expressed as a sum over all pairs of atoms in the system as follows (in the notation of the original paper):

$$E_{disp}^{D3(BJ)} = -\frac{1}{2} \sum_{A \neq B} \left(s_6 \frac{C_6^{AB}}{R_{AB}^6 + [f(R_{AB}^0)]^6} + s_8 \frac{C_8^{AB}}{R_{AB}^8 + [f(R_{AB}^0)]^8} \right) \quad (24)$$

Here, s_6 and s_8 are fit parameters specific to each functional. C_n^{AB} is the averaged dispersion coefficient of order n for the pair of atoms A and B, and R_{AB} is their internuclear distance. The damping function $f(R_{AB}^0)$ is defined by $f(R_{AB}^0) = a_1 R_{AB}^0 + a_2$, with a_1 and a_2 fit parameters specific to each functional, and R_{AB}^0 a cut-off distance specific to each pair of atoms A and B.

2.2.6 Relativistic corrections

The zeroth-order regular approximation (ZORA)[25–27] is a formalism developed for approximate treatment of relativistic effects. It results from a transformation of the four-component Dirac equation to a two-component form, with regular expansion to zeroth order of the resulting Hamiltonian. Within the Kohn-Sham formalism, ZORA effectively leads to a change in equation (11), yielding a new set of one electron equations:

$$\left(V_{KS} + \hat{p} \cdot \frac{c^2}{2c^2 - V_{KS}} \hat{p} + \frac{c^2}{(2c^2 - V_{KS})^2} \hat{\sigma} \cdot (\nabla V_{KS} \times \hat{p}) \right) \chi_i = \epsilon_i \chi_i \quad (25)$$

where $\hat{p}$ is the momentum operator, c the speed of light, and $\hat{\sigma}$ the Pauli matrices. The third term in the parenthesis on the left side of equation (25) corresponds to the spin-orbit coupling. Neglecting this term yields the scalar-relativistic ZORA formalism.

2.3 Orbital localization

A wave function described by a single Slater determinant remains invariant under unitary transformation of its constituent single-electron orbitals. In particular, in the context of Kohn-Sham DFT, this means that a different basis for the space spanned by the Kohn-Sham orbitals may be chosen without altering the electron density. The motivation for this could for instance be to obtain a set of orbitals which allow for easier qualitative chemical interpretation.

An example of a scheme to obtain a set of transformed orbitals is the one presented by Boys and Foster in 1960 [14]. The resulting orbitals may be called *localized orbitals*, as a possible interpretation of the method is the minimization of their spatial extent. These orbitals could be attractive to chemists, as the picture they provide often corresponds to

16

chemical intuition due to their localization.

Given a set of one-electron orbitals χ_i, for instance those obtained in the Kohn-Sham procedure, an orthonormal set of linear combinations of these orbitals can be expressed as

$$\chi_j^* = \sum_i c_{ji} \chi_i \tag{26}$$

where χ_j^* is the jth orbital in the new set, and c_{ji} is a coefficient in the linear combination. The new orbitals should be chosen so that orthonormality is preserved, $\langle \chi_i^* | \chi_j^* \rangle = \delta_{ij}$. The centroid of charge of an orbital, $\vec{R}_i$, is given by

$$\vec{R}_i = \langle \chi_i^* | \vec{r} | \chi_i^* \rangle \ . \tag{27}$$

The localized orbitals in the Boys-Foster scheme are then defined to be those that maximize the following expression

$$\prod_{i>j} |\vec{R}_i - \vec{R}_j|^2 \ , \tag{28}$$

where the product runs over all unique pairs of orbitals.

2.4 Electronegativity equalization

Electronegativity equalization [15] is a method used to obtain atomic charges, often for use in molecular mechanics or molecular dynamics simulations. An atom i is described by an atomic electronegativity ξ_i and an atomic chemical hardness η_i. Atomic charges q_i are then assigned to the different atoms in the system so as to equalize the chemical potential of the electrons everywhere in the molecule. The potential energy V of the molecule is expressed as

$$V = \sum_i \left(\xi_i q_i + \frac{1}{2} \eta_i q_i^2 + \frac{1}{2} \sum_{j \neq i} \frac{q_i q_j}{r_{ij}} + \phi_i q_i \right) , \tag{29}$$

where r_{ij} is the distance between two atoms i and j, and ϕ_i is the value of an external electrostatic potential at the position of atom i. A set of atomic charges is then sought which minimize V subject to the constraint $\sum_i q_i = 0$ (for a neutral system). This problem may be solved using the method of Lagrangian multipliers by minimizing the quantity L defined by

$$L = V + \mu \sum_i q_i \tag{30}$$

where μ is a Lagrangian multiplier. Differentiating equation (30) with respect to an atomic charge q_k and the Lagrangian multiplier μ yields the following partial derivatives:

$$\frac{\partial L}{\partial q_k} = \xi_k + \phi_k + \eta_k q_k + \sum_{j \neq k} \frac{q_j}{r_{jk}} + \mu \tag{31}$$

$$\frac{\partial L}{\partial \mu} = \sum_i q_i \tag{32}$$

The set of equations to be solved for the atomic charges is then obtained by setting each partial derivative equal to zero, resulting in the equations

$$0 = \xi_k + \phi_k + \eta_k q_k + \sum_{j \neq k} \frac{q_j}{r_{jk}} + \mu , \quad k \in \{1, 2, 3...N\} \tag{33}$$

$$0 = \sum_i q_i \tag{34}$$

with N being the number of atoms in the system. Note that this is a set of linear equations, solvable by standard techniques of linear algebra.

2.4.1 The Au$_{20}$ cluster

Electronegativity equalization may be used to derive expressions for the atomic charges in a tetrahedral Au$_{20}$ cluster. The symmetry of the cluster may be exploited to simplify the set of equations to be solved. There are three distinct types of symmetry-equivalent atoms in the cluster, namely *vertex*, *edge* and *face* atoms. Figure 2.1 shows a tetrahedral Au$_{20}$ cluster and defines these atom type labels.

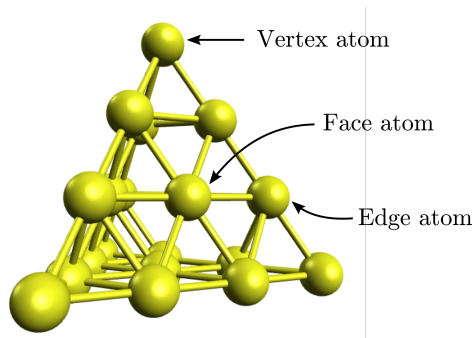*Figure 2.1: A tetrahedral Au$_{20}$ cluster with different atom type labels indicated.*

Atoms of the same type are expected to have the same electronegativity, hardness and charge in the electronegativity equalization framework. To arrive at a set of equations describing the cluster, some approximations are made. A regular tetrahedron is assumed, with all nearest-neighbour bond lengths equal to the same value r, henceforth

called the characteristic bond length of the cluster. As will be seen in the results section, this is not necessarily the minimum geometry of the structure. However, such a cluster can be constructed and used in calculations, hence this is not so much an approximation as a choice about the kind of theoretical system to be studied. Secondly, Coulomb interactions other than those between nearest neighbours are neglected, and the Coulomb interactions are described by a simple $\frac{1}{r}$ dependence rather than including shielding corrections. For the sake of clarity, the following list describes which atoms were considered nearest neighbours for each atom type:

- Vertex atom: the three closest edge atoms.

- Edge atom: the closest vertex atom, the edge atom on the same edge, the two edge atoms neighbouring the same vertex atom, and the two face atoms on the faces which meet to form the edge the atom is a part of.

- Face atom: the six edge atoms on the same face, and the three other face atoms.

Given the aforementioned approximations, and in the absence of an external electric potential, equations (33) and (34) reduce to the following set of only 4 equations:

$$0 = \xi_v + \eta_v q_v + \frac{3q_e}{r} + \mu \tag{35}$$

$$0 = \xi_e + \eta_e q_e + \frac{q_v + 2q_f + 3q_e}{r} + \mu \tag{36}$$

$$0 = \xi_f + \eta_f q_f + \frac{6q_e + 3q_f}{r} + \mu \tag{37}$$

$$0 = 4q_v + 4q_f + 12q_e \tag{38}$$

where subscripts v, e and f indicate variables describing a vertex, edge or face atom, respectively. This set of equations can be solved analytically for the atomic charges, yielding

$$q_v = \frac{r^2 \left(\eta_e \xi_f - \eta_e \xi_v + 3\eta_f \xi_e - 3\eta_f \xi_v\right) + r \left(6\xi_e - 6\xi_f\right)}{r^2 \left(\eta_e \eta_f + \eta_e \eta_v + 3\eta_f \eta_v\right) + r \left(3\eta_e - 3\eta_f\right) - 12} \tag{39}$$

$$q_e = -\frac{r^2 \left(\eta_f \xi_e - \eta_f \xi_v + \eta_v \xi_e - \eta_v \xi_f\right) + r \left(3\xi_e - \xi_f - 2\xi_v\right)}{r^2 \left(\eta_e \eta_f + \eta_e \eta_v + 3\eta_f \eta_v\right) + r \left(3\eta_e - 3\eta_f\right) - 12} \tag{40}$$

$$q_f = -\frac{r^2 \left(\eta_e \xi_f - \eta_e \xi_v - 3\eta_v \xi_e + 3\eta_v \xi_f\right) + r \left(-3\xi_e - 3\xi_f + 6\xi_v\right)}{r^2 \left(\eta_e \eta_f + \eta_e \eta_v + 3\eta_f \eta_v\right) + r \left(3\eta_e - 3\eta_f\right) - 12}. \tag{41}$$

Alternatively, these expressions could be written in terms of differences in electronegativity by introducing $\Delta_{ij}\xi = \xi_i - \xi_j$. Making this substitution and some basic simplifications,

one obtains

$$q_v = \frac{r\left(\eta_e \Delta_{fv}\xi + 3\eta_f \Delta_{ev}\xi\right) + 6\Delta_{ef}\xi}{r\left(\eta_e\eta_f + \eta_e\eta_v + 3\eta_f\eta_v\right) + 3\left(\eta_e - \eta_f\right) - \frac{12}{r}} \tag{42}$$

$$q_e = -\frac{r\left(\eta_f \Delta_{ev}\xi + \eta_v \Delta_{ef}\xi\right) + \left(2\Delta_{ev}\xi + \Delta_{ef}\xi\right)}{r\left(\eta_e\eta_f + \eta_e\eta_v + 3\eta_f\eta_v\right) + 3\left(\eta_e - \eta_f\right) - \frac{12}{r}} \tag{43}$$

$$q_f = -\frac{r\left(\eta_e \Delta_{fv}\xi + 3\eta_v \Delta_{fe}\xi\right) + 3\left(\Delta_{ve}\xi + \Delta_{vf}\xi\right)}{r\left(\eta_e\eta_f + \eta_e\eta_v + 3\eta_f\eta_v\right) + 3\left(\eta_e - \eta_f\right) - \frac{12}{r}}. \tag{44}$$

2.4.2 Au$_{20}$ in a homogeneous electric field

As in the previous section, an Au$_{20}$ cluster with a regular tetrahedron structure is considered, with a characteristic bond length r. For a homogeneous electric field of strength E parallel to the z-axis, the external potential ϕ_i is given by $\phi_i = -Ez_i$, where z_i is the z-coordinate of atom i. The reference point of zero potential is chosen to be the origin for convenience. The cluster is assumed to be aligned so that a face atom is placed at the origin, and the opposite vertex atom is placed along the positive z-axis. For such an alignment, the cluster may be considered to consist of four levels, where all atoms on each level experience the same electric potential due to their equal z-displacements. This labeling is shown in figure 2.2.
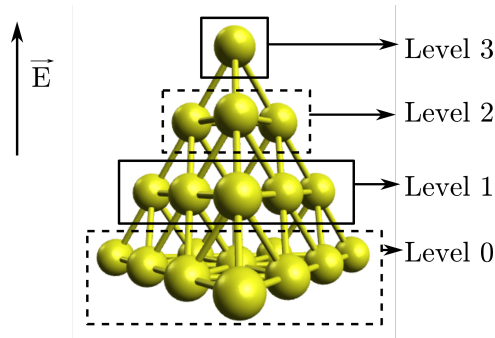
Figure 2.2: The alignment of the tetrahedral Au$_{20}$ cluster relative to the direction of the electric field is shown, as well as the terminology used to describe groups of atoms placed at different displacements along the z-axis. The z-axis is parallel to the indicated direction of the field.

Due to the symmetry of the cluster, simple geometric considerations mean the distance in the z-direction between two adjacent levels may be expressed in terms of r as $\sqrt{\frac{2}{3}}r$. The electronegativity and chemical hardness of an atom of a certain type (vertex, edge or face) is assumed to be the same regardless of which level in the cluster it is on, but the charge will of course have a specific value for each combination of level and atom type. The charge is represented by q_{tl}, where the subscripts t and l denote an atom type and a level, respectively. The atom type subscripts are as before (v for vertex, e for edge, f for face),

while the level subscript runs from 0 to 3, 0 denoting the level with the lowest z-value and 3 the one with the highest (fig. 2.2). Once again neglecting Coulomb interactions other than those between nearest neighbours, the above considerations reduce the set of equations given by (33) and (34) to the following:

$$0 = -\sqrt{6}Er + \eta_v q_{v3} + \mu + \frac{3q_{e2}}{r} + \xi_v \tag{45}$$

$$0 = -\frac{2E}{3}\sqrt{6}r + \eta_e q_{e2} + \mu + \xi_e + \frac{1}{r}\left(q_{e1} + 2q_{e2} + 2q_{f1} + q_{v3}\right) \tag{46}$$

$$0 = -\frac{Er}{3}\sqrt{6} + \eta_e q_{e1} + \mu + \xi_e + \frac{1}{r}\left(2q_{e0} + q_{e2} + 2q_{f1} + q_{v0}\right) \tag{47}$$

$$0 = -\frac{Er}{3}\sqrt{6} + \eta_f q_{f1} + \mu + \xi_f + \frac{1}{r}\left(2q_{e0} + 2q_{e1} + 2q_{e2} + q_{f0} + 2q_{f1}\right) \tag{48}$$

$$0 = \eta_v q_{v0} + \mu + \xi_v + \frac{1}{r}\left(2q_{e0} + q_{e1}\right) \tag{49}$$

$$0 = \eta_e q_{e0} + \mu + \xi_e + \frac{1}{r}\left(2q_{e0} + q_{e1} + q_{f0} + q_{f1} + q_{v0}\right) \tag{50}$$

$$0 = \eta_f q_{f0} + \mu + \xi_f + \frac{1}{r}\left(6q_{e0} + 3q_{f1}\right) \tag{51}$$

$$0 = 6q_{e0} + 3q_{e1} + 3q_{e2} + q_{f0} + 3q_{f1} + 3q_{v0} + q_{v3} \tag{52}$$

These equations may be solved analytically for the charges, but the resulting expressions are rather involved. Interested readers are referred to appendix A, where the full solution is given. The main result is that the charges are expected to vary linearly with the electric field strength:

$$q_{tl} \propto E \tag{53}$$

3 Method

The technical details of the computations performed in this project will be presented in the following chapter. A method validation study is presented, leading to the choice of computational methodology to be used for the rest of the calculations. The setup of subsequent calculations performed in the result-generating phase of the project is described in detail. The software Amsterdam Density Functional (ADF, version 2014.10) [28–30] was used for all calculations. Some additional technical details, e.g. input settings, are given in appendix B.

3.1 Method validation

To find a suitable DFT method for the project at hand, a method validation study comparing several exchange-correlation functionals was conducted. Inclusion of dispersion corrections and relativistic effects (both scalar-relativistic and spin-orbit coupling) was also considered. This was done by running geometry optimizations on Au_2 and the rhombus isomer of Au_4 and comparing the resulting cohesive energies and bond lengths to experimental data where available, otherwise to high quality theoretical calculations from the literature. For Au_4, the bond length between two adjacent atoms following the edge of the cluster is the one considered. Basis set convergence was also checked by running the calculations with increasingly large basis sets, including some computationally efficient frozen core basis sets. Cohesive energies $E_{cohesive}$ were calculated according to

$$E_{cohesive} = \frac{n \cdot E(\text{Au}) - E(\text{Au}_n)}{n},$$
(54)

that is, the energy $E(\text{Au})$ of an unbound gold atom times the number n of atoms in the cluster, minus the energy $E(\text{Au}_n)$ of the cluster, divided by the number of gold atoms. The energy of an unbound atom was found from an unrestricted single point calculation, with doublet spin state specified. The cohesive energy may be interpreted as the binding energy per atom of the cluster.

Two GGA functionals were included in the validation study, namely PBE [18] and S12g [31], as well as the two meta-GGA functionals M06-L [21, 22] and TPSS [19, 20]. None of these are hybrid functionals, meaning the increased computational cost associated with the calculation of nonlocal Hartree-Fock exchange is avoided. PBE [32], M06-L[33, 34] and TPSS[35] were chosen for their previously reported success in calculations on gold clusters. Meanwhile, S12g is a relatively new functional which has not seen much use in calculations on gold. It has however been used for other transition metals in similar applications [36], hence it represents an interesting option to consider. PBE and TPSS

were considered both with and without Grimme's dispersion correction, DFT-D3(BJ)[24]. In the former case, they were labeled PBE-D3 and TPSS-D3 respectively. Note that S12g already includes a Grimme-type dispersion correction in its parameterization, while M06-L, being heavily parameterized, is expected to include dispersion effects by virtue of its parameterization. Initially, relativistic effects were treated using the ZORA approach [25–27] at the scalar-relativistic level. Relativistic effects are known to be important for gold [4], hence calculations without any treatment of them are not considered a relevant option. The built-in basis sets in ADF [16] designed for use with ZORA were employed. The basis sets TZ2P and QZ4P were tested in combination with all the chosen exchange-correlation functionals. In addition, TZ2P frozen core basis sets freezing orbitals up to and including the 4d and 4f subshells (labeled TZ2P.4d and TZ2P.4f, respectively) were tested for PBE-D3. Results for the different quantities calculated in the validation study are shown in tables 3.1, 3.2, 3.3 and 3.4.

Table 3.1: Cohesive energies for Au_2 in eV *for different combinations of exchange-correlation functional, basis set and dispersion correction.*

	TZ2P.4f	TZ2P.4d	TZ2P	QZ4P
S12g	1.052	1.058	1.048	1.056
PBE			1.148	1.157
PBE-D3	1.169	1.175	1.168	1.177
TPSS			1.141	1.148
TPSS-D3			1.169	1.175
M06-L			1.128	1.139
Exp. [37, 38]				1.16

Table 3.2: Cohesive energies for Au_4 in eV *for different combinations of exchange-correlation functional, basis set and dispersion correction.*

	TZ2P.4f	TZ2P.4d	TZ2P	QZ4P
S12g			1.357	1.369
PBE			1.516	1.581
PBE-D3	1.582	1.589	1.570	1.585
TPSS			1.523	1.538
TPSS-D3			1.600	1.615
M06-L			1.529	1.536
CCSD(T) [34]				1.578

Table 3.3: Bond lengths for Au₂ in Å for different combinations of exchange-correlation functional, basis set and dispersion correction.

	TZ2P.4f	TZ2P.4d	TZ2P	QZ4P
S12g	2.563	2.559	2.561	2.558
PBE			2.524	2.519
PBE-D3	2.528	2.523	2.524	2.519
TPSS			2.513	2.508
TPSS-D3			2.512	2.508
M06-L			2.539	2.538
Exp. [37, 38]				2.472

Table 3.4: Bond lengths for Au₄ in Å for different combinations of exchange-correlation functional, basis set and dispersion correction.

	TZ2P.4f	TZ2P.4d	TZ2P	QZ4P
S12g			2.732	2.727
PBE			2.691	2.675
PBE-D3	2.687	2.683	2.689	2.684
TPSS			2.679	2.674
TPSS-D3			2.677	2.671
M06-L			2.714	2.710
CCSD(T) [34]				2.648

A graphical presentation of the data from the validation study is given in figures 3.1 and 3.2. These show the errors in the calculated quantities relative to the reference values from the literature, calculated as

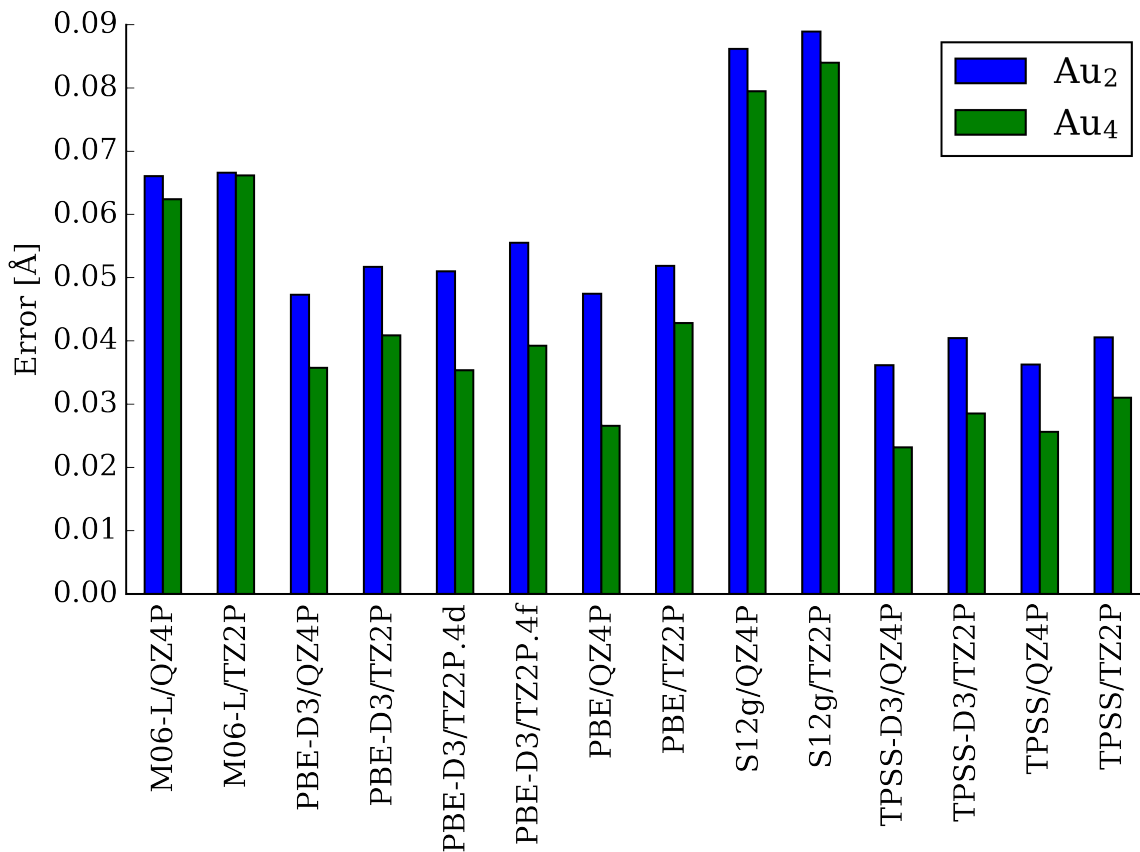Error = Calculated value from this work - Reference value.

Figure 3.1: For different combinations of exchange-correlation functional and basis set, the figure shows errors in calculated bond lengths for Au2 and Au4 relative to reference values [34, 37, 38] from the literature.

Considering the bond length errors in figure 3.1, TPSS seems to perform best among the chosen functionals, followed by PBE. S12g yields significantly higher errors than the other functionals, while M06-L falls somewhere in between PBE and S12g. Regarding basis sets, QZ4P gives a slight improvement over TZ2P, but the difference is small enough to consider TZ2P as sufficiently converged, especially considering the significant increase in computational effort required to use QZ4P. The frozen core basis sets TZ2P.4d and TZ2P.4f perform similarly to their all-electron counterpart. The effect of including a dispersion correction is not large enough to draw any reasonable conclusion about the importance of its inclusion.
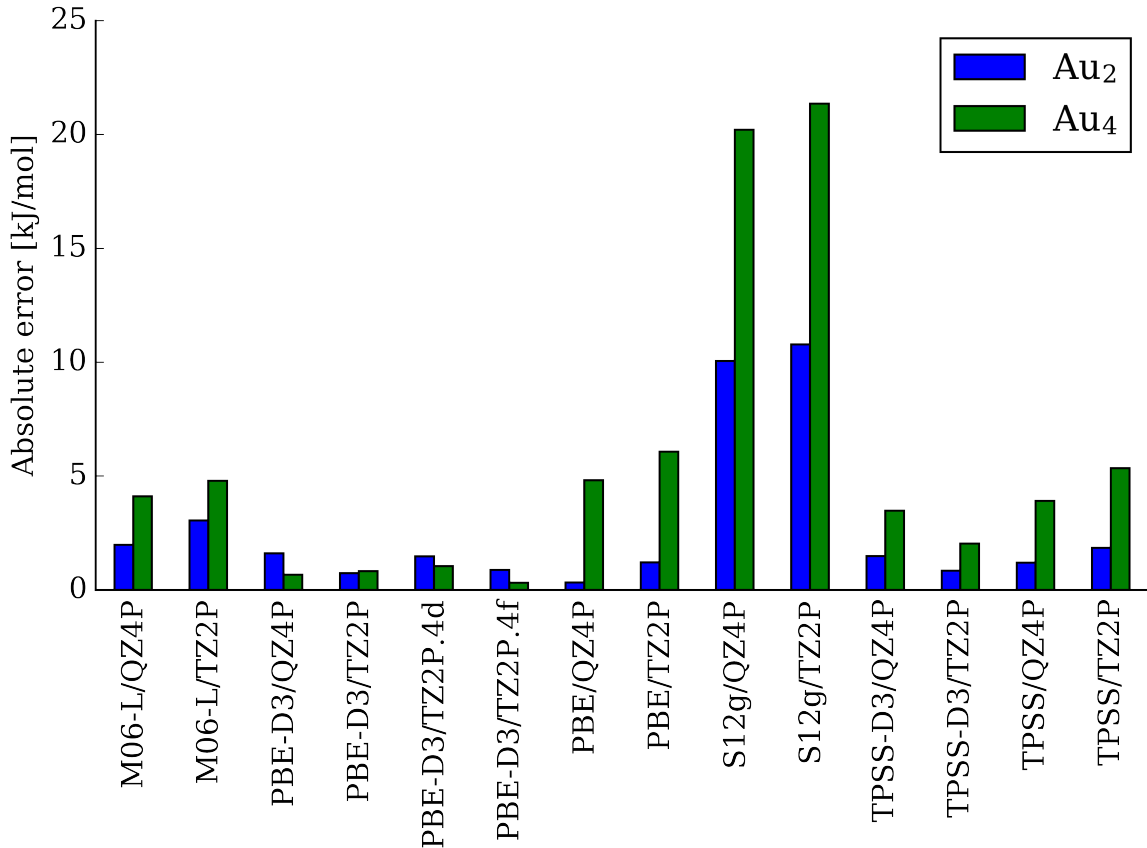
Figure 3.2: For different combinations of exchange-correlation functional and basis set, the figure shows errors in calculated cohesive energies for Au_2 and Au_4 relative to reference values [34, 37, 38] from the literature.

Considering the cohesive energy errors in figure 3.2, S12g once again has the highest errors. M06-L, TPSS and PBE all show errors of approximately the same magnitude for Au_4, while the differences are slightly larger for Au_2, with PBE having the smallest errors for the latter species. Including a dispersion correction yields a significant improvement in the Au_4 errors for PBE. As a consequence of this, PBE-D3 yields the overall best performance. Once again, frozen core basis sets perform similarly to the all-electron variant. Slight differences are observed upon increasing the basis set size from TZ2P to QZ4P, but not enough to justify the associated increase in computational effort.

As a final test, the first singlet-triplet excitation energy of Au_{20} was computed for each of the functionals using time-dependent density functional theory (TDDFT) as implemented in ADF [39]. This was done to include a property of a somewhat larger cluster in the validation study, with the specific choice of property being due to the availability of an experimental value [40] for comparison. The results are presented in table 3.5.

Table 3.5: First singlet-triplet excitation energy of Au₂₀ in eV, calculated using different exchange-correlation functionals.

Method	$\Delta E_{singlet-triplet}$ [eV]
PBE/TZ2P.4d	1.752
S12g/TZ2P.4d	1.793
TPSS/TZ2P	1.792
M06-L/TZ2P	1.870
Exp.[40]	1.77

As may be seen in table 3.5, M06-L performs significantly worse than the other functionals with a relatively large deviation from the experimental value. PBE underestimates the excitation energy, while TPSS and S12g overestimate it, but in terms of absolute errors these three functionals show similar performance.

Based on the above considerations, PBE-D3/TZ2P.4d is chosen as the method to be used for calculations in this work. PBE-D3 shows the best performance on cohesive energies, but is second to TPSS-D3 when considering the bond lengths. However, a pragmatic factor is the availability of frozen core basis sets in ADF. These are unavailable for use with mGGA-functionals, hence PBE-D3 allows significant computational savings relative to TPSS-D3, making it the best overall choice. Based on the calculations in the validation study, the use of a frozen core basis does not seem to impact the results negatively to a significant degree. Increasing the basis set size to QZ4P is not deemed necessary; while this yields a slight increase in accuracy, the gain is not large enough to justify the increased computational cost. As a side note, the dispersion correction is expected to be important for the description of nonbonding interactions between gold clusters and molecules, hence there is an additional point in favor of its inclusion which is not revealed by the numbers considered here.

3.1.1 Spin-orbit coupling

For the chosen DFT-method, PBE-D3/TZ2P.4d, some additional calculations were performed to assess the necessity of including spin-orbit coupling in subsequent calculations. The energy difference ΔE_{SO} given by the following formula was calculated both with and without spin-orbit coupling:

$$\Delta E_{SO} = E(\text{Au}_4) - 2E(\text{Au}_2) \tag{55}$$

In equation (55), $E(\text{X})$ denotes the energy of chemical species X. Hence, ΔE_{SO} may be interpreted as dissociation energy of the gold tetramer relative to two gold dimers.

Optimized structures were used in the energy calculations. This quantity is chosen rather than e.g. a simple cohesive energy to avoid the complications of open-shell spin-orbit calculations. The obtained values are given in table 3.6. Also given in the table is CPU time usage from a single point calculation on an Au_{20} cluster, conducted as a simple timing test.

Table 3.6: *The energy difference ΔE_{SO} in eV, calculated with and without spin-orbit coupling, as well as the CPU time usage in a single point calculation on an Au_{20}-cluster.*

ZORA level	ΔE_{SO} [eV]	CPU time Au_{20}
Scalar	-1.66	30min
Spin-orbit	-1.82	3h48min

The values in table 3.6 differ by 0.16eV, a significant amount. However, the single point calculation shows a nearly 8-fold increase in CPU time usage with the inclusion of spin-orbit coupling. Due to the large increase in computational cost, spin-orbit coupling is therefore neglected, even though inclusion of the effect could mean a significant increase in accuracy. Scalar-relativistic ZORA will be used to treat relativistic effects in all calculations.

3.2   Description of calculations

3.2.1   Gold cluster geometry optimizations

Geometry optimizations were performed for Au_2, Au_4, Au_{20} and Au_{58}. The calculations on Au_2 and Au_4 were part of the validation study, while Au_{20} and Au_{58} were chosen for their reported stability in the literature [9, 40]. The input geometries for each calculation are given in appendix C.1. For Au_4, only the rhombus structure was investigated. That is, the optimization was started from a rhombus structure, with the symmetry point group of the input conserved throughout the optimization. Au_{20} is known to possess a tetrahedral structure [41], hence the optimization was started from such a geometry, but without symmetry constraints. For Au_{58}, a core-shell structure was constructed to resemble that reported in [9], with a single gold atom as the core, 11 atoms in the first shell, and 46 atoms in the second shell. This structure was then used as input in the geometry optimization.

3.2.2 Charge distribution in Au$_{20}$

To study the charge distribution in gold clusters, Au$_{20}$ was chosen as a model system. Its highly symmetric structure means a model can be developed for the charges, as done in section 2.4, while the system still has a certain size. An idealized regular tetrahedron structure was used, not necessarily corresponding to the actual minimum geometry. This is a structure of exactly the kind considered in the derivations in section 2.4. Single point calculations were run for 20 different regular tetrahedron Au$_{20}$ clusters, each of them with a characteristic bond length corresponding to one of 20 equally spaced points on the interval $[2.523\,\text{Å}, 2.88\,\text{Å}]$. The lower and upper endpoints of the interval correspond to the shortest Au–Au bond length in the gold dimer (as obtained from the geometry optimization in this work) and bulk gold [42], respectively. From these calculations, Hirshfeld charges were obtained for each atom.

The cartesian coordinates of each gold atom in a regular tetrahedron Au$_{20}$ cluster with a given characteristic bond length were produced as follows: A coordinate system was introduced defined by three vectors of length equal to the desired bond length, each of which points from a vertex of the tetrahedron in the direction of one of the other vertices. In this basis, the set $\{(i, j, k) \mid i, j, k \in \{0, 1, 2, 3\}, \quad i + j + k \leq 3\}$ specifies the positions of all gold atoms in the cluster. These coordinates are then transformed to the cartesian coordinate system, yielding the input geometry for the single point calculation.

To study the effect of an electric field, a regular tetrahedron Au$_{20}$ cluster with characteristic bond length equal to 2.7 Å was constructed as described in the previous paragraph. The structure was then aligned so that a face atom was positioned at the origin, and the opposite vertex atom was placed along the z-axis. Note that this structure and alignment is what is assumed in the derivation in section 2.4. 21 single point calculations were run, each of which had a homogeneous external electric field directed along the z-axis. Each calculation used a different field strength, given by 21 equally spaced points on the interval $[0.0, 0.02]$, where the field strengths are in atomic units. Hirshfeld charges were obtained for each atom from these calculations.

3.2.3 Interaction between Au$_{20}$ and CO

The interaction between an Au$_{20}$ cluster and CO was chosen for further study. This choice was made due to substantial interest in CO oxidation catalyzed by gold in the literature [3]. The specific choice of the Au$_{20}$ cluster was made as its structure is well established [40, 41], while it is also large enough to have several possible adsorption sites. Only a "standing" bonding mode was considered in this work, that is, with CO bonding to gold through the carbon atom, and the oxygen atom pointing away from the cluster.

Ten possible coordination sites were identified, these are shown in figure 3.3. They fall into three different categories: *atop*, *bridge* and *hollow*. An atop site has the molecule placed directly above a gold atom, a bridge site has it placed between two atoms, and a hollow site has it placed in the hollow between three atoms. In abstract terms, each site consists of a point and a vector, henceforth referred to as *site point* and *site vector*. The site point lies on the surface of the cluster, while the site vector points away from it and specifies the line along which the diatomic molecule should be placed. Hence, the precise specification of each site boils down to the specification of these two geometric constructs. A detailed specification of each distinct site is given in appendix D.
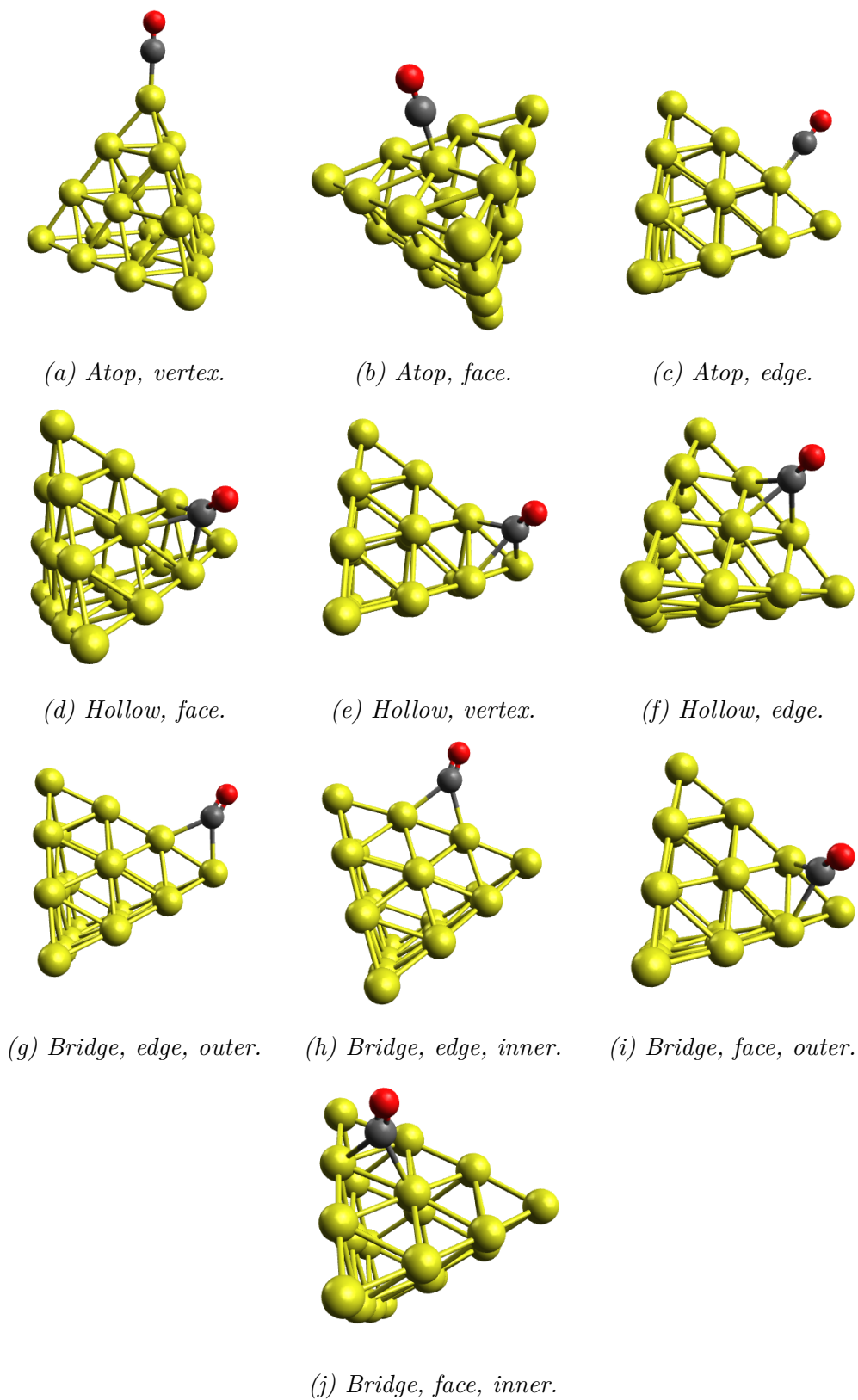
(a) Atop, vertex.

(b) Atop, face.

(c) Atop, edge.

(d) Hollow, face.

(e) Hollow, vertex.

(f) Hollow, edge.

(g) Bridge, edge, outer.

(h) Bridge, edge, inner.

(i) Bridge, face, outer.

(j) Bridge, face, inner.

Figure 3.3: Different possible coordination sites on the surface of an Au_{20} cluster for the adsorption of a CO molecule.

Initially, a potential energy surface scan was performed by running single point calculations with CO placed at different distances from a chosen coordination site on the surface of the cluster. For each site, a calculation was run for each of 41 distances corresponding to equally spaced points on the interval $[1.0\,\text{Å}, 3.0\,\text{Å}]$. Input geometries for these calculations were obtained by taking the previously optimized geometry of the Au_{20} cluster, and then placing the carbon atom the specified distance from the relevant site point in the direction of the site vector. The oxygen atom was then placed a further $1.137\,\text{Å}$ (bond length of CO in the optimized geometry obtained in this work) from the carbon atom in the direction specified by the site vector.

For each site, a constrained geometry optimization was subsequently performed using the geometry from the potential energy surface scan with CO placed a distance of $2.0\,\text{Å}$ from the site as input geometry. The carbon and oxygen atoms of CO were allowed to move along the line through the site point in the direction of the site vector. All other coordinates were frozen, that is, all gold atoms as well as the coordinates of carbon and oxygen corresponding to displacement perpendicular to the aforementioned line. Unconstrained geometry optimizations were then run using the final geometries from the constrained optimizations as input geometries, to check which geometries correspond to actual minima when the structure is allowed to relax completely. For the sites found to be stable minima, a number of additional calculations were then run to get some desired characteristics of the systems. These included:

- A calculation of the vibration frequencies of the $Au_{20}-CO$ complex, so as to determine the CO stretch frequency and to confirm the stationary point as an actual minimum.

- Two separate single point calculations, one on Au_{20} and one on CO, each with the geometry that subsystem has in the optimized structure of the complex. The purpose of these calculations was to obtain binary result files for each subsystem which may then be given as input to a new single point calculation on the whole system using the fragment functionality of ADF. Briefly, this amounts to using the orbitals from each fragment as a basis in the calculation on the whole system. The advantage of doing this is that electron populations for the basis functions can be obtained from the output. As these basis functions are now effectively the molecular orbitals of CO and Au_{20}, populations for e.g. the HOMO and LUMO of CO are obtained, providing a useful analysis tool. For each basis function, the gross population is calculated as a sum over all molecular orbitals of the product between the occupation of each molecular orbital and the contribution (percentage) of the basis function to that molecular orbital.

- A single point calculation for each subsystem, CO and Au_{20}, using the structure it has in the optimized geometry of the complex and the basis of the full system. These calculations enable determination of the basis set superposition error.

4 Results and discussion

4.1 Gold cluster geometry optimizations

The optimized geometries of Au_2, the rhombus isomer of Au_4, Au_{20} and Au_{58} are presented in this section. Cartesian coordinates of the optimized structures are given in appendix C.2. The geometries will not be discussed in detail, as the main objective of the geometry optimizations was simply to obtain minimum geometries for subsequent calculations, but they are still presented for completeness. Selected high-energy localized molecular orbitals of some of the clusters are also discussed to gain qualitative insight into the bonding in the clusters. The localized orbitals are used in place of the ones obtained directly from the Kohn-Sham procedure as the delocalized nature of the latter make simple qualitative interpretation more difficult.

4.1.1 Au_2

A bond length of 2.523 Å was obtained in the optimized structure of the gold dimer, shown in figure 4.1.

Figure 4.1: Optimized structure of Au_2.

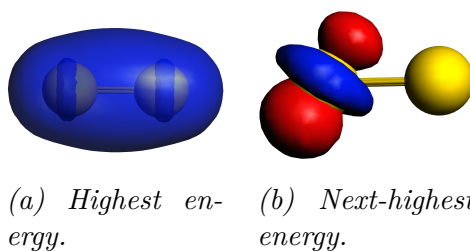The two highest-energy occupied localized molecular orbitals (MOs) of the dimer are shown in figure 4.2.

(a) Highest energy.   *(b) Next-highest energy.*

Figure 4.2: Highest-energy occupied localized molecular orbitals of Au_2.

4.1.2 Au_4

The optimized structure of the rhombus isomer of Au_4 is shown in figure 4.3.
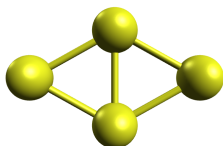
Figure 4.3: Optimized structure of the rhombus isomer of Au$_4$.

The highest-energy occupied localized molecular orbitals of Au4 are shown in figure 4.4.

(a) Highest energy. (b) Next-highest energy. (c) Third-highest energy.

Figure 4.4: Highest-energy occupied localized molecular orbitals of Au$_4$.

4.1.3 Au$_{20}$

The optimized structure of the Au$_{20}$ cluster is shown in figure 4.5.

Figure 4.5: Optimized structure of Au$_{20}$.

Some of the occupied localized molecular orbitals of highest energy for Au$_{20}$ are shown in figure 4.6.

(a) One of the ten highest-energy localized MOs.   *(b) One of the ten highest-energy localized MOs.*   *(c) The 11th-highest-energy localized MO.*
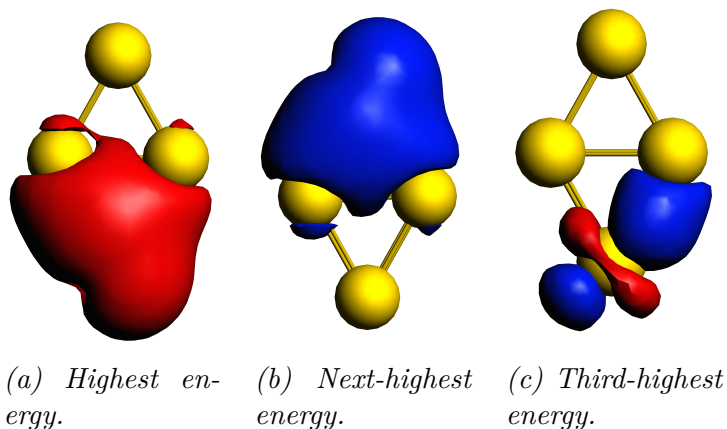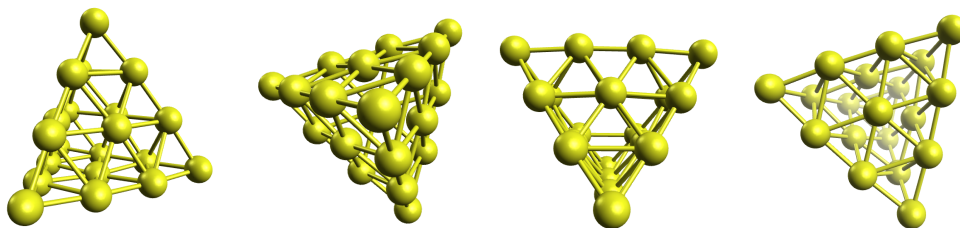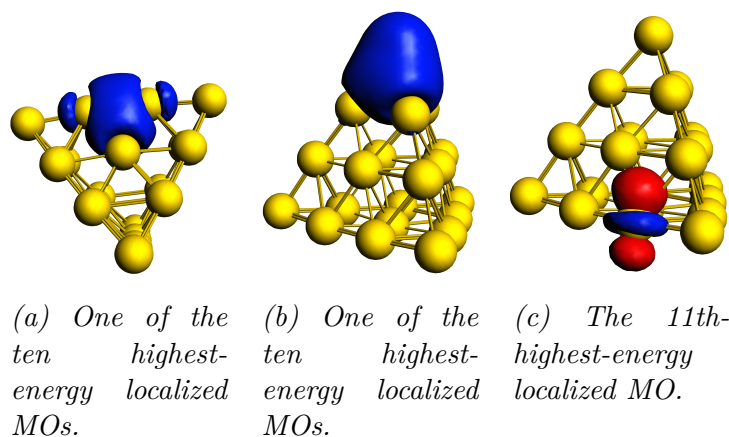
Figure 4.6: Highest-energy occupied localized molecular orbitals of Au₂₀.

4.1.4 Au58

The optimized structure of the Au58 cluster is shown in figure 4.7.

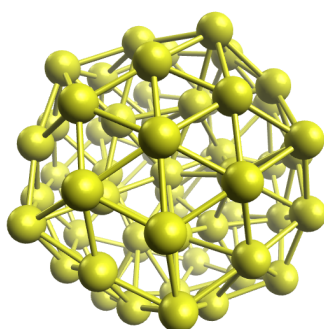*Figure 4.7: Optimized structure of Au58.*

4.1.5 Discussion of orbitals

The orbitals of Au2, Au4 and Au20 shown in figures 4.2, 4.4 and 4.6 respectively all reveal the same qualitative pattern. The highest-energy $\frac{n}{2}$ (n being the number of gold atoms in the cluster) of the occupied localized molecular orbitals all have shapes which could have been formed as linear combinations of atomic s-orbitals, and they are all bonding. For each cluster, these orbitals would be sufficient to accommodate the unpaired 6s electrons from the constituent atoms in the cluster. The orbitals of energy lower than these bonding MOs look more like d-orbitals localized on single atoms, and do not exhibit the same bonding character, at least not to the same degree. It is emphasized that this is a purely qualitative and rather simplistic consideration, but it could be considered as an

36

indication that the 6s electrons are important for the bonding in the clusters, a conclusion which agrees with chemical intuition given the electronic configuration of a gold atom.

4.1.6 Cohesive energies

The cohesive energies of the optimized structures of Au_2, rhombus Au_4, Au_{20} and Au_{58} are given in table 4.1.

Table 4.1: Cohesive energies for optimized structures of selected gold clusters.

Cluster	Cohesive energy [eV]
Au_2	1.175
Au_4	1.589
Au_{20}	2.542
Au_{58}	2.899

The cohesive energy is seen to increase with increasing number of gold atoms in the cluster. The difference per added atom seems to be larger for small clusters; the difference between the cohesive energies of Au_2 and Au_4 is of the same order of magnitude as the difference between Au_{20} and Au_{58}, even though the former differ by only two atoms, compared to 38 for the latter two. This could possibly indicate that the increase in cohesive energy with size eventually levels off, reaching a limiting value as the structures become more similar to that of bulk gold. This is in agreement with the trend seen in reference [32].

4.2 Charge distribution in Au_{20}

4.2.1 Variation of atomic charges with characteristic bond length

As described in section 3.2.2, single point calculations were performed on regular tetrahedron Au_{20} clusters of different characteristic bond length. The variation in the Hirshfeld charge of different atom types with characteristic bond length is shown in figure 4.8.
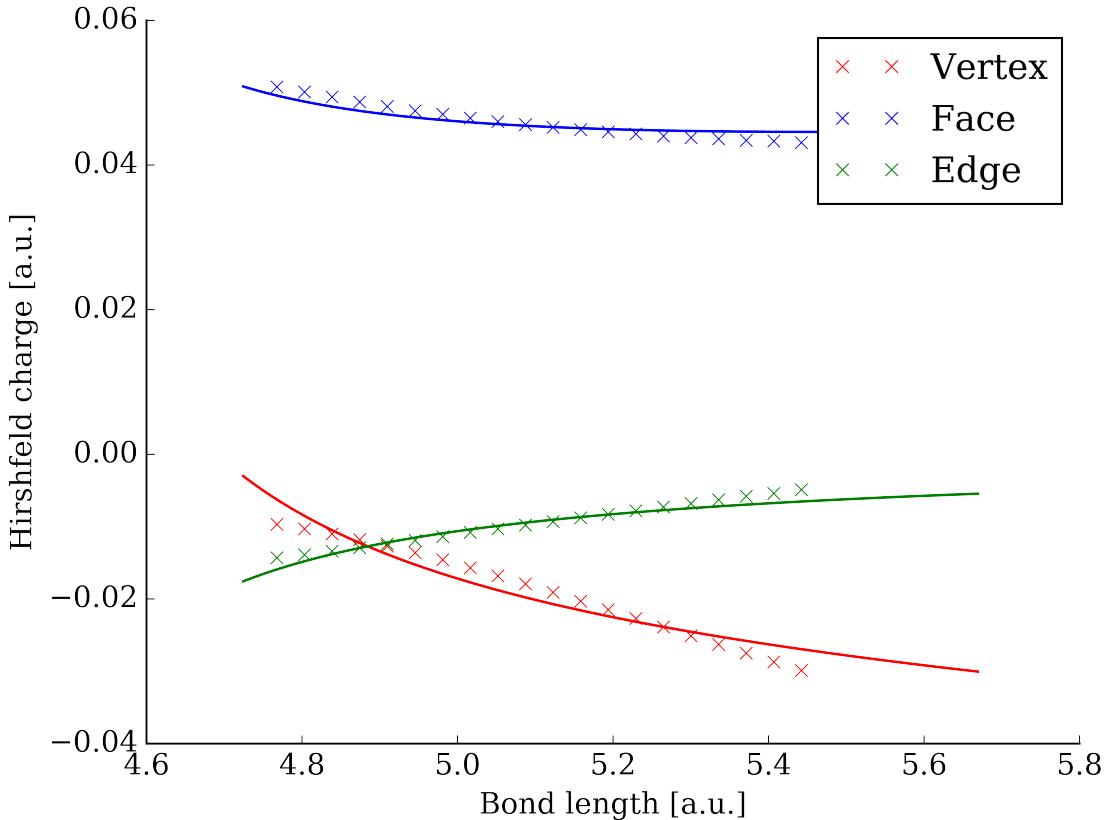
Figure 4.8: Variation in Hirshfeld charge of different atom types in a regular tetrahedron Au₂₀ cluster, for different choices of characteristic bond length. The data points are results from DFT-calculations, while the lines show a curve fitting of equations (42), (43) and (44) to these points.

The atomic charges plotted in figure 4.8 are all relatively small. Still, the plot shows a number of interesting features worthy of discussion. The face atoms are positively charged, while the edge and vertex atoms have negative charge for all bond lengths. This could indicate a tendency to increase the electron density around atoms of lower coordination at the expense of more highly coordinated atoms. The vertex atoms become more negatively charged as the characteristic bond length becomes longer, while the edge atoms become less negatively charged. The face atoms become less positively charged for higher bond lengths.

Equations (42), (43) and (44) were fit to the data from the DFT-calculations. As the equations are nonlinear, the fit parameters were found by minimizing a sum of squared residuals using the basinhopping algorithm [43] for global optimization, with the BFGS algorithm used for local minimization in each basinhopping step. The trends are reproduced well by the fit model, but there are some discrepancies. Most importantly, the

curvature of the lines corresponding to vertex and edge atoms seems to be opposite that of the DFT data. Still, the fit is relatively good given the simple nature of the electronegativity equalization model. Additionally, a better set of fit parameters could well exist, as there is no way of knowing if the actual global minimum was found by the basinhopping algorithm. The parameters used for the plot in figure 4.8 are given in table 4.2 for completeness, but they should probably not be subjected to too much interpretation, as other minima of similar fit quality with quite different parameters were also observed.

Table 4.2: Parameters for a fit of equations (42), (44) *and* (43) *to the data from DFT calculations presented in figure 4.8.*

Parameter	Value [a.u.]
η_v	0.03747
η_e	0.81456
η_f	0.20662
$\Delta_{fv}\xi$	-0.03093
$\Delta_{ev}\xi$	-0.00721
$\Delta_{ev}\xi$	0.02319

The good fit of the electronegativity equalization model to the DFT data has some interesting implications. The whole model rests on the assumption that different atom types have different electronegativities and hardnesses. However, the atoms in the cluster are all gold atoms. Hence, this indicates that the electronegativity and hardness parameters also depend on some additional characteristics of the system. The different coordination numbers of the different atom types could play a role, as the electronegativity equalization framework takes the geometry of the cluster into account through the Coulomb interactions.

4.2.2 Effect of an electric field

As described in section 3.2.2, the effect of an electric field on the charge distribution in the Au_{20} cluster was studied by running single point calculations on a regular tetrahedron Au_{20} structure in a homogeneous external electric field, each calculation run with a different field strength. The resulting charges of different atoms in the cluster for different field strengths are plotted in figure 4.9.
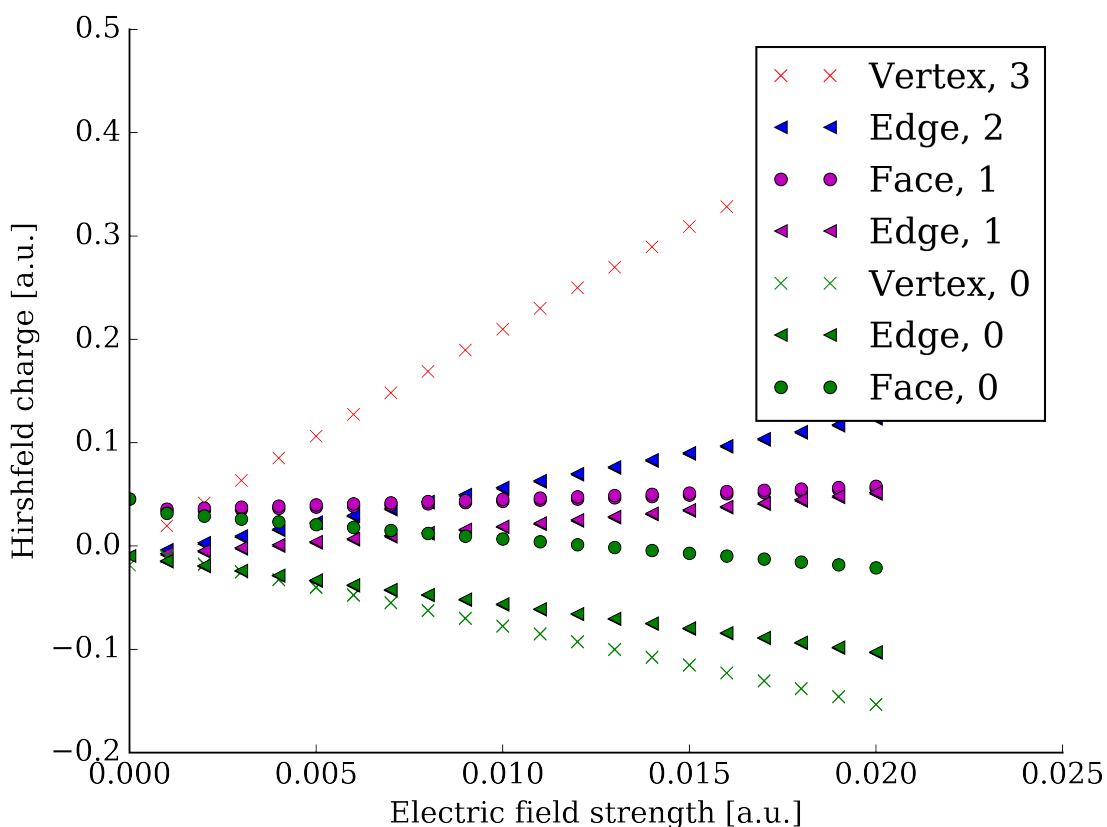
Figure 4.9: The variation in Hirshfeld charge for different atom types in a regular tetrahedron Au$_{20}$ cluster for different electric field strengths. See section 2.4 for a description of the curve labels.

The Hirshfeld charges are seen to vary linearly with the field strength for all atom types. This is as expected from the model developed in section 2.4. As the field strength is increased, negative charge builds up in the base level of the cluster, while atoms positioned closer to the other end of the cluster become more positive. Note also that the atomic charges induced by the electric field are significantly larger in absolute value than those observed in the absence of a field in figure 4.8.

4.3   Interaction between Au$_{20}$ and CO

4.3.1   CO

Results from a geometry optimization of a single CO molecule are shown in table 4.3.

(a) 5σ-orbital of (HOMO).
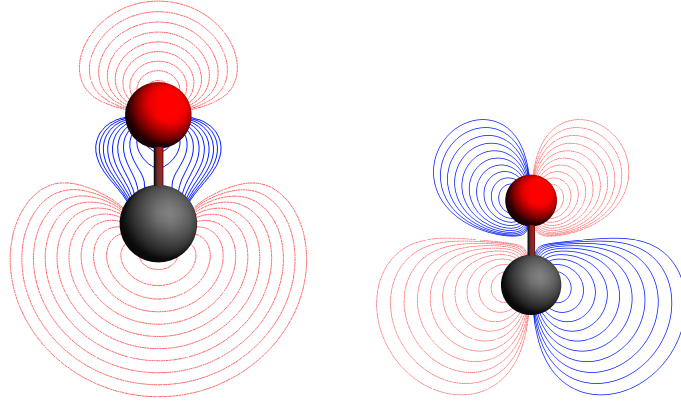
(b) $2\pi^*$-orbital (LUMO).

Figure 4.10: Contour plots of the HOMO and LUMO of CO. Solid/blue and dashed/red lines correspond to opposite signs. C and O are rendered in black and red, respectively.

Table 4.3: Bond length, vibration frequency of the C-O stretch, and Hirshfeld charges of the C and O atoms from an optimized geometry of the CO-molecule.

Bond length [Å]	1.137
C-O stretch frequency [cm^{-1}]	2123.9
Hirshfeld charge, oxygen [a.u.]	-0.0732
Hirshfeld charge, carbon [a.u.]	0.0731

The highest occupied and lowest unoccupied molecular orbitals (HOMO and LUMO) of CO as obtained from the Kohn-Sham procedure are shown in figure 4.10.

The HOMO and LUMO, 5σ and $2\pi^*$ respectively, play central roles in the description of the reactivity of CO [44]. Note their spatial distribution, with the electron density shifted towards the carbon atom.

4.3.2 Potential surface scan

As described in section 3.2.3, single point energy calculations were carried out on a system consisting of a single CO atom and a Au_{20} cluster to investigate the shape of the potential energy surface for adsorption to different types of coordination sites. The adsorption energy E_{ads} was calculated for each distance considered, defined as the difference between the energy of the interacting system and the sum of the energies of its subsystems:

$$E_{ads} = E(Au_{20}-CO) - (E(Au_{20}) + E(CO)) \tag{56}$$

Results for different site types are shown in figures 4.11, 4.12 and 4.13. It is emphasized that these are results from single point calculations, hence the results show only the variation in adsorption energy with a single geometric degree of freedom.

Figure 4.11: Adsorption energy for CO coordinated to atop-type sites on a Au_{20}-cluster, plotted against the distance between the two fragments measured between the coordination site on the surface of the cluster and the carbon atom in CO.

Figure 4.11 shows the variation in adsorption energy with distance for atop-type sites. Distinct minima are observed for adsorption to vertex and edge atoms, while the minimum for coordination to a face atom is more subtle due to the curve flattening after reaching its minimum value. Note that all atop-type sites yield negative adsorption energy values, that is, adsorption is energetically favourable. The strength of the adsorption increases from face to edge to vertex, as seen by the increasingly negative values. A possible explanation for this trend could be the lower degree of steric crowding, as the number of nearest neighbours of the gold atom at the coordination site decreases in the same order.
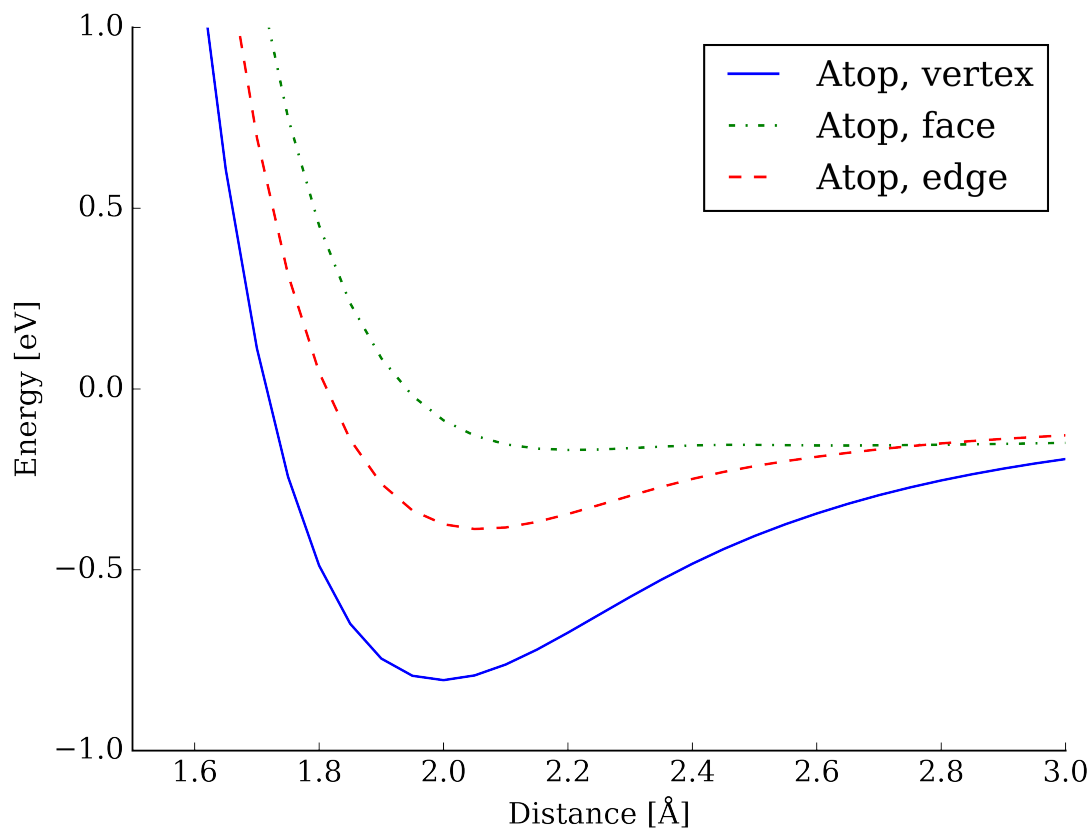
Figure 4.12: Adsorption energy for CO coordinated to hollow-type sites on a Au_{20}-cluster, plotted against the distance between the two fragments measured between the coordination site on the surface of the cluster and the carbon atom in CO.

Variation in adsorption energy with distance for hollow-type sites is shown in figure 4.12. The curves have similar shapes for all the individual sites considered, but the curve for the face site is shifted to lower energies compared to the other two. Note that the curves are all monotonically decreasing, lacking any distinct minima, but reaching favourable (negative) values of the adsorption energy when the distance gets large enough.
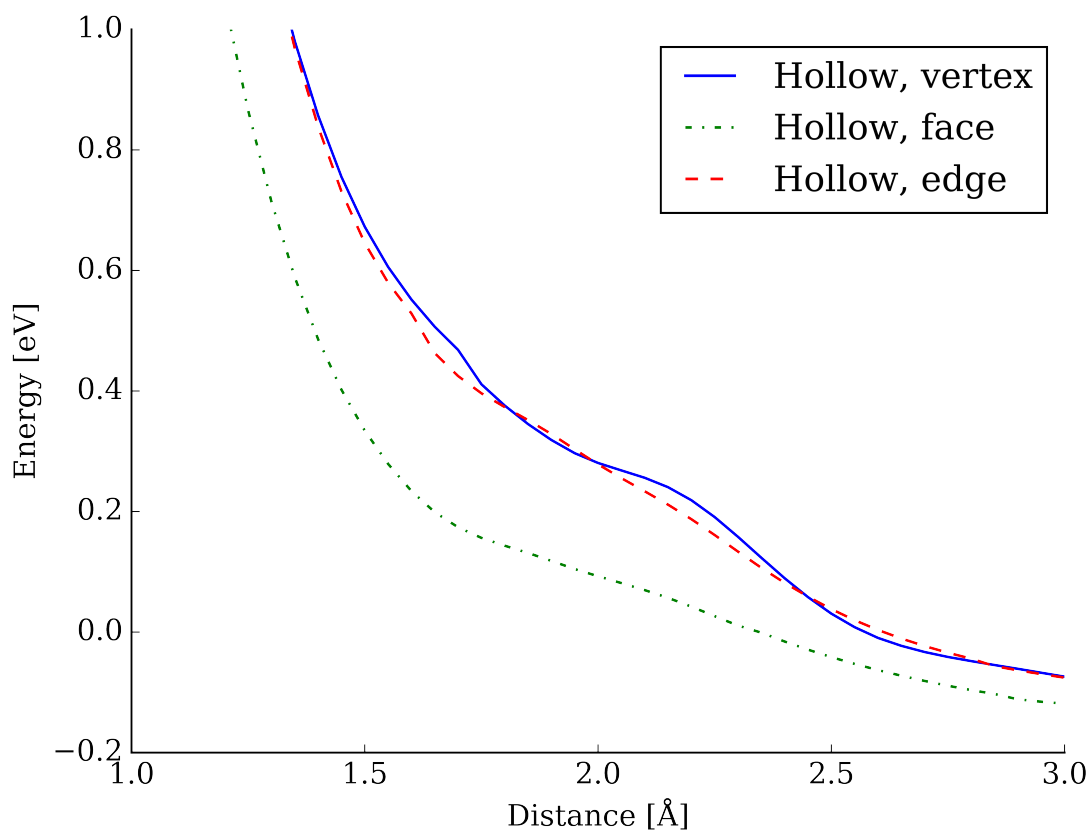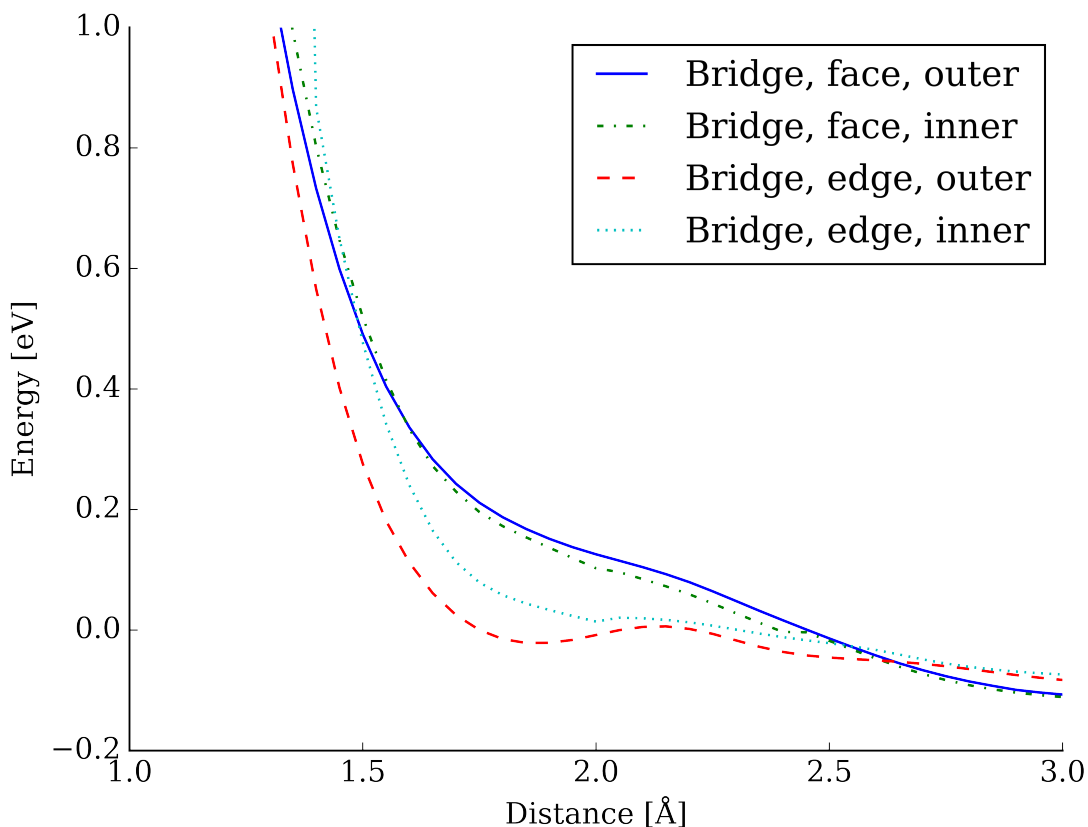
Figure 4.13: Adsorption energy for CO coordinated to bridge-type sites on a Au$_{20}$-cluster, plotted against the distance between the two fragments measured between the coordination site on the surface of the cluster and the carbon atom in CO.

For the bridge-type sites, the variation in adsorption energy with distance between the two subsystems is shown in figure 4.13. There seems to be a distinction between the bridge sites on the edge and the face of the cluster, with the curves for the sites on the face lacking any local minima, while the edge site curves have some subtle local minima. However, these are rather shallow, and should probably not be assigned too great significance. Like the hollow-type sites, the bridge-type sites also yield negative adsorption energies at large distances.

4.3.3   Geometry optimizations

Following the preliminary study of the potential energy surface of the Au$_{20}$–CO system, the different coordination sites were subjected to further investigation by running constrained geometry optimizations. The constrained optimizations converged for all sites. The resulting structures were then submitted as input geometries to unconstrained

geometry optimizations to determine which of them correspond to actual minima.

Of the different coordination sites considered, only the atop-type sites were found to be stable minima, albeit with some structural distortion compared to the structures from the constrained optimizations. Both the optimizations started from bridge-type and hollow-type sites converged to atop-type sites. The final geometries from the unconstrained optimizations of the atop-type sites are shown in figures 4.14, 4.15 and 4.16.

Figure 4.14: *The final geometry of the Au_{20}–CO system after unconstrained geometry optimization, with CO adsorbed to a face atom in an atop site.*
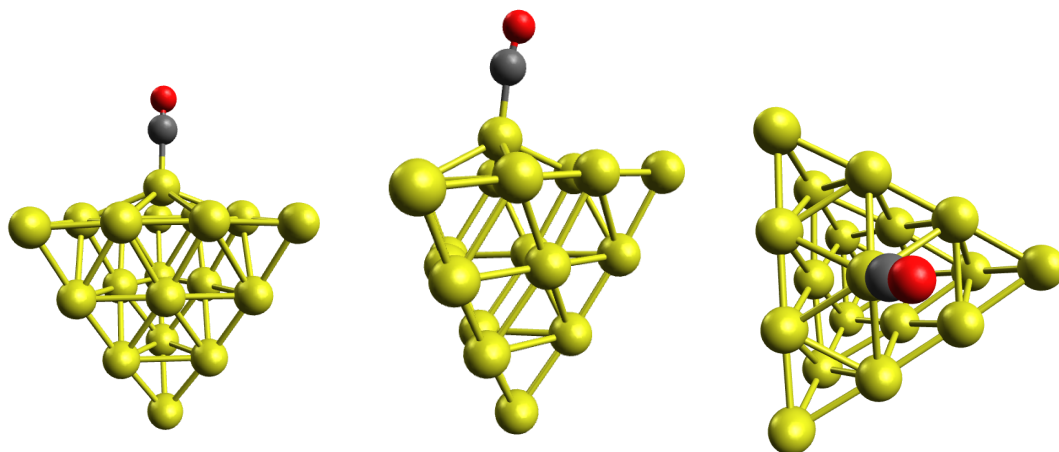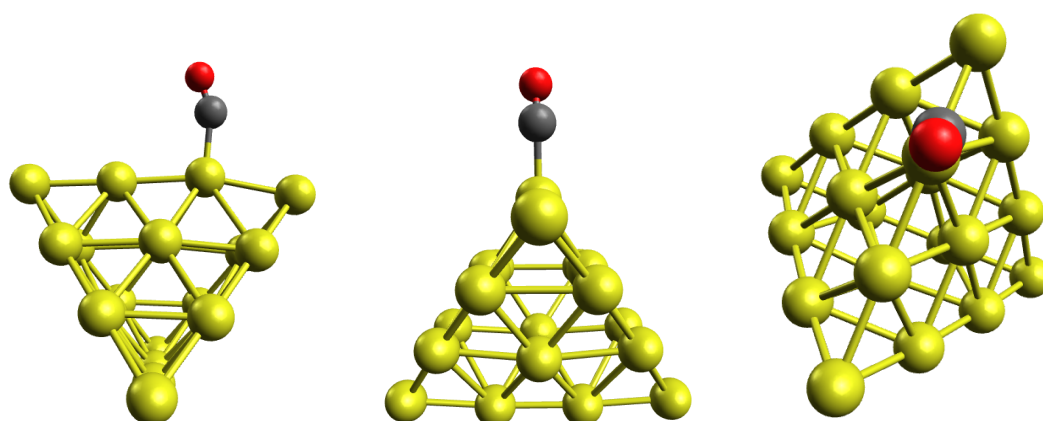

Figure 4.15: *The final geometry of the Au_{20}–CO system after unconstrained geometry optimization, with CO adsorbed to an edge atom in an atop site.*
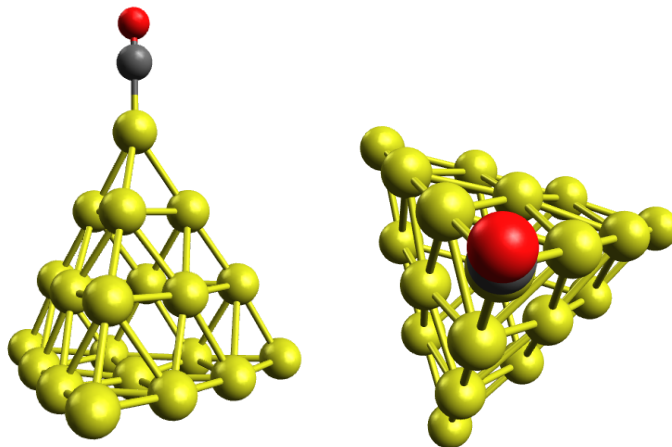
Figure 4.16: The final geometry of the Au₂₀–CO system after uncon-strained geometry optimization, with CO adsorbed to a vertex atom in an atop site.

Qualitatively, after optimization the final geometries can all still be considered to fall within the atop category, in spite of some structural distortion. These were all confirmed to be actual minima, as no imaginary frequencies were obtained from computation of the vibration frequencies. For adsorption to a face atom (figure 4.14), the most prominent geometric change observed is that the face atom itself has moved to a position above the plane of the initial surface of the cluster. Furthermore, CO is not perpendicular to the triangular face of the cluster, but oriented at a slight angle to a line perpendicular to the plane of the face. Considering adsorption to an edge atom (4.15), some structural distortion can also be observed in the cluster. Once again the atom which carbon coordinates to seems to remove itself slightly from the cluster, making a dent in the otherwise symmetric edge. CO tilts toward the midpoint of the edge. Adsorption in the vertex position qualitatively seems to be causing the least amount of structural distortion of the cluster. CO is once again oriented at a slight angle to a line pointing straight from the cluster.

A number of quantities were calculated for the optimized structures. These include some structural variables, the BSSE-corrected adsorption energy, the CO stretch vibration frequency, electron populations for the 5σ and $2\pi^*$ orbitals of CO, and the Hirshfeld charges of the C and O atoms. The results are presented in table 4.4.

Table 4.4: Computed properties of Au_{20}–CO systems with CO adsorbed in different atop-type sites, namely to a vertex, edge or face atom. Where relevant, previously presented results for unadsorbed CO are included for comparison. The adsorption energies have been corrected for BSSE.

	Atop, vertex	Atop, edge	Atop, face	Free CO
Au–C bond length [Å]	1.979	2.027	1.990	
C–O bond length [Å]	1.144	1.147	1.145	1.137
Au–C–O angle [°]	175.9	157.2	171.1	
CO stretch frequency [cm^{-1}]	2061.7	2025.3	2051.8	2123.9
CO 5σ population	1.65	1.67	1.65	2.00
CO $2\pi_x^*$ population	0.15	0.14	0.16	0.00
CO $2\pi_y^*$ population	0.15	0.19	0.16	0.00
Adsorption energy [eV]	-0.862	-0.535	-0.441	
Hirshfeld charge, C [a.u.]	0.11	0.08	0.10	0.0731
Hirshfeld charge, O [a.u.]	-0.05	-0.07	-0.07	-0.0732

The strongest adsorption is found for coordination to a vertex atom, with an adsorption energy of -0.862eV. This is substantially more than for the edge and face atoms, which yield -0.535eV and -0.441eV, respectively.

The shortest Au–C bond is found for the vertex site, while the edge site has the longest.

Considering the bond length of CO, a longer bond than in the free molecule is observed for all coordination sites. The differences between the sites are rather small, but still noticeable, with the vertex site yielding the shortest CO bond at 1.144Å. The face site has a barely longer bond at 1.145Å, while the edge site yields the longest bond at 1.147Å. These lengths seem to correlate with the vibration frequency of the CO stretch, which is red-shifted as the bond grows longer. While free CO has a frequency of 2123.9 cm^{-1}, frequencies of 2061.7 cm^{-1}, 2025.3 cm^{-1} and 2051.8 cm^{-1} are observed for CO adsorbed to a vertex, edge or face atom respectively. Both of these effects - the elongation of the CO bond and the red-shift in the stretch frequency - can probably be traced to π-backbonding. The gold cluster donates electrons to the antibonding virtual $2\pi^*$-orbital of CO, hence weakening the CO bond, which results in a longer bond with a lower vibration frequency. There is an increasing degree of π-backbonding on going from a vertex site to a face site to an edge site, as evidenced by the increasing electron population in the $2\pi_x^*$- and $2\pi_y^*$-orbitals of CO. A complementary orbital effect is σ-donation from the 5σ-orbital of CO, observable as a reduction of the electron population in this orbital when the molecule adsorbs to the gold cluster. While the orbital is occupied by 2 electrons in free CO, the population is reduced to 1.65 upon adsorption to a vertex or face atom. The

σ-donation is weaker for adsorption to an edge atom, as evidenced by the slightly higher 5σ population, 1.67.

While the populations of the $2\pi^*$ orbitals would suggest that the adsorption should be stronger for the face site than the vertex site due to the stronger π-backbonding, as previously mentioned a substantially lower adsorption energy is obtained for adsorption to the vertex atom, $-0.862\,\mathrm{eV}$ compared to $-0.441\,\mathrm{eV}$. A possible explanation could be that CO experiences additional steric repulsion as a consequence of the more crowded surroundings of the face atom compared to the vertex atom. An additional point is the structural distortion of the cluster, which will be accompanied by an energy penalty as the cluster deviates from its minimum geometry. The distortion is considerably more pronounced upon adsorption to the face site than to the vertex site. The adsorption energy for the edge atom is intermediate between the two other sites. While coordination to this site provides the greatest backdonation of electron density to the $2\pi^*$-orbitals, the σ-donation is slightly weaker than for the other two sites, making it difficult to reason about the exact balance struck between these two changes working in opposite directions. However, steric repulsion and structural distortion could be possible explanations for this site's position between the two others in terms of adsorption energy, as both the degree of crowding around the interacting gold atom and the extent of structural distortion qualitatively seems to be intermediate between the two other sites.

A final point to note is the change in Hirshfeld charges in the CO molecule observed upon adsorption, namely a shift towards more positive values. This mainly affects the carbon atom for adsorption to an edge or face atom, with the strongest effect seen for the face site. In the vertex site, oxygen is also affected, and the carbon atom has its most positive value among all the sites. Note that this implies net transfer of electrons from CO to Au_{20} for all the sites.

Qualitatively, the effects of σ-donation and π-backbonding may be observed by studying the shape of the molecular orbitals in the interacting system. Application of a localization procedure is beneficial for this purpose, as the rather delocalized nature of the orbitals obtained from the Kohn-Sham procedure make interpretation more difficult. A few selected localized molecular orbitals are shown in figures 4.17, 4.18 and 4.19 for adsorption to a vertex, edge or face atom respectively.

(a) π-backbonding.   *(b) σ-donation.*
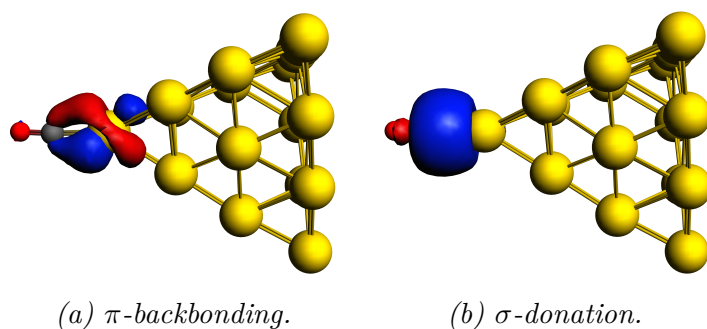
Figure 4.17: Localized molecular orbitals showing orbital interactions associated with adsorption of CO to a vertex atom of an Au$_{20}$ cluster.

(a) π-backbonding.   *(b) π-backbonding.*   *(c) σ-donation.*
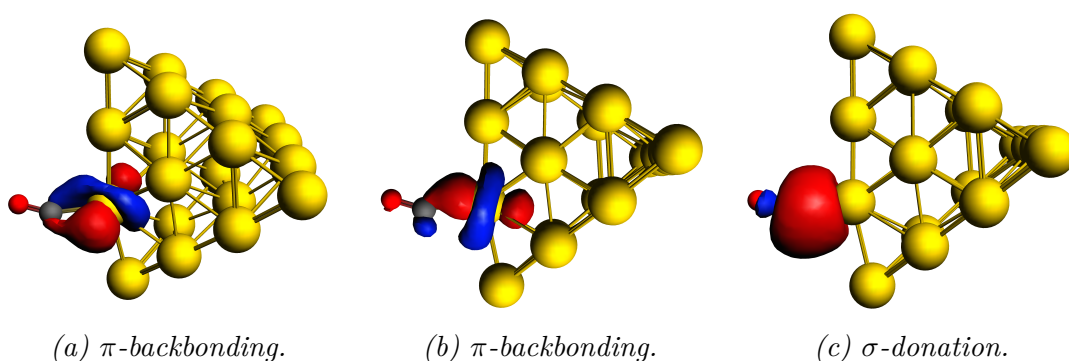
Figure 4.18: Localized molecular orbitals showing orbital interactions associated with adsorption of CO to an edge atom of an Au$_{20}$ cluster.

(a) π-backbonding.   *(b) σ-donation.*
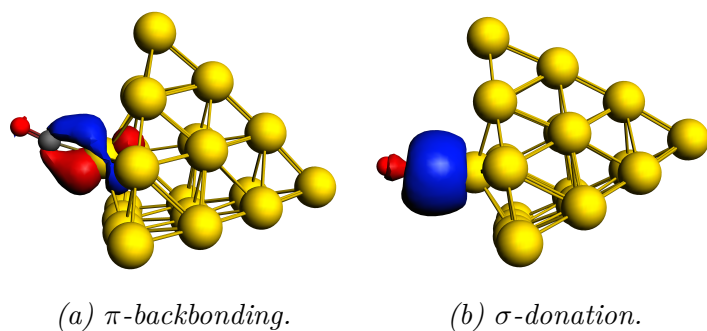
Figure 4.19: Localized molecular orbitals showing orbital interactions associated with adsorption of CO to a face atom of an Au$_{20}$ cluster.

The orbitals in figures 4.17b, 4.18c and 4.19b resemble each other, with approximate σ-symmetry and distinct bonding character between the C and Au atoms, as seen from the lack of nodes between the two atoms. They all have contributions from the 5σ-orbital of CO, hence they provide a qualitative picture of the σ-donation to the Au$_{20}$ cluster.

The orbitals shown in figures 4.17a, 4.18a and 4.19a also have similar shapes. They all have approximate π-symmetry around the Au–C bond, with no nodal planes perpendicular to the interatomic axis. Their expansions in basis functions all include the $2\pi^*$-orbitals of CO, thus they could be interpreted as a qualitative picture of the π-backbonding from Au$_{20}$ to these antibonding orbitals on CO.

The orbital shown in figure 4.18b deserves special mention. While the orbitals which may be interpreted as contributing to π-backbonding all have shapes similar to those shown in figures 4.17a and 4.19a for adsorption to a vertex or face atom, one of the π-backbonding orbitals seen upon adsorption to an edge atom has the shape shown in figure 4.18b. This could be interpreted as an explanation of the distinct tilt of CO in this system, as this structural change appears to align one of the lobes of a $2\pi^*$-orbital of CO so as to facilitate donation from the Au$_{20}$ cluster.

5 Conclusion

A validation study was conducted to choose a suitable DFT method for the study of small gold clusters, resulting in the choice of the PBE functional with Grimme's DFT-D3(BJ) dispersion correction, a TZ2P basis set with a frozen core including subshells up to and including 4d, and a treatment of relativistic effects by the scalar-relativistic ZORA formalism. Optimized geometries and cohesive energies were obtained for a handful of gold clusters (Au_2, Au_4, Au_{20} and Au_{58}). The cohesive energies were seen to increase with increasing cluster size. For a regular tetrahedron Au_{20} cluster, a model for the atomic charges was developed using electronegativity equalization, both in the presence and absence of an electric field. The model for the case without an electric field was fit to atomic charges obtained from DFT calculations with different characteristic bond lengths for the cluster. The variation of the atomic charges of a Au_{20} cluster with field strength of a homogeneous electric field was also studied. The charges were seen to vary linearly with the field strength, in agreement with the prediction of the electronegativity equalization model. Several possible adsorption sites for the interaction between the Au_{20} cluster and CO were investigated. CO was found to adsorb only to atop-type sites. The adsorption was strongest for gold atoms of low coordination number. A redshift in the $C-O$ stretch vibration frequency was observed in the adsorbed molecules.

6 References

[1] G. J. Hutchings, M. Brust, H. Schmidbaur, *Chemical Society reviews* **2008**, *37*, 1759–1765.

[2] M. Haruta, *Nature* **2005**, *437*, 1098–1099.

[3] G. J. Hutchings, M. Haruta, *Applied Catalysis A: General* **2005**, *291*, 2–5.

[4] P. Pyykkö, *Angewandte Chemie - International Edition* **2004**, *43*, 4412–4456.

[5] P. Pyykkö, *Inorganica Chimica Acta* **2005**, *358*, 4113–4130.

[6] P. Pyykkö, *Chemical Society reviews* **2008**, *37*, 1967–1997.

[7] H. Häkkinen, *Chemical Society Reviews* **2008**, *37*, 1847.

[8] B. Assadollahzadeh, P. Schwerdtfeger, *Journal of Chemical Physics* **2009**, *131*, 64306.

[9] W Huang, M Ji, C. D. Dong, X Gu, L. M. Wang, X. G. Gong, L. S. Wang, *Acsnano* **2008**, *2*, 897–904.

[10] P. Schwerdtfeger, M. Lein, R. P. Krawczyk, C. R. Jacob, *Journal of Chemical Physics* **2008**, *128*, 124302.

[11] H.-C. Fang, Z. H. Li, K.-N. Fan, *Physical Chemistry Chemical Physics* **2011**, *13*, 13358–13369.

[12] P. Hohenberg, W. Kohn, *Physical Review* **1964**, *136*, B864–B871.

[13] W Kohn, L. J. Sham, *Physical Review* **1965**, *140*, 1133–1138.

[14] J. M. Foster, S. F. Boys, *Reviews of Modern Physics* **1960**, *32*, 300–302.

[15] A. K. Rappé, W. A. Goddard III, *Journal of Physical Chemistry* **1991**, *95*, 3358–3363.

[16] E. Van Lenthe, E. J. Baerends, *Journal of Computational Chemistry* **2003**, *24*, 1142–1156.

[17] S. Boys, F Bernardi, *Molecular Physics* **1970**, *19*, 553–566.

[18] J. P. Perdew, K. Burke, M. Ernzerhof, *Phys. Rev. Lett.*, Phys. Rev. Lett. (USA) **1996**, *77*, 3865–3868.

[19] V. N. Staroverov, G. E. Scuseria, J. Tao, J. P. Perdew, *Journal of Chemical Physics* **2003**, *119*, 12129–12137.

[20] J. Tao, J. P. Perdew, V. N. Staroverov, G. E. Scuseria, *Physical Review Letters* **2003**, *91*, 146401.

[21] Y. Zhao, D. G. Truhlar, *Journal of Chemical Physics* **2006**, *125*, DOI 10.1063/1.
      2370993.

[22] Y. Zhao, D. G. Truhlar, *Theoretical Chemistry Accounts* **2008**, *120*, 215–241.

[23] P. J. Stephens, F. J. Devlin, C. F. Chabalowski, M. J. Frisch, *The Journal of
      Physical Chemistry* **1994**, *98*, 11623–11627.

[24] S. Grimme, S. Ehrlich, L. Goerigk, *Journal of Computational Chemistry* **2011**, *32*,
      1456–1465.

[25] E. V. Lenthe, E. J. Baerends, J. G. Snijders, *The Journal of Chemical Physics*
      1993, *99*, 4597.

[26] E. van Lenthe, E. J. Baerends, J. G. Snijders, *The Journal of Chemical Physics*
      1994, *101*, 9783.

[27] E. Van Lenthe, A. Ehlers, E.-J. Baerends, *The Journal of Chemical Physics* **1999**,
      110, 8943.

[28] Amsterdam Density Functional, Theoretical Chemistry, Vrije Universiteit, Amster-
      dam, The Netherlands.

[29] G. te Velde, F. M. Bickelhaupt, E. J. Baerends, C. Fonseca Guerra, S. J. a. van
      Gisbergen, J. G. Snijders, T. Ziegler, G. T. E. Velde, C. F. Guerra, S. J. a. V. a. N.
      Gisbergen, *Journal of Computational Chemistry* **2001**, *22*, 931–967.

[30] C. Fonseca Guerra, J. G. Snijders, G. Te Velde, E. J. Baerends, *Theoretical Chem-
      istry Accounts: Theory Computation and Modeling (Theoretica Chimica Acta)* **1998**,
      99, 391–403.

[31] M. Swart, *Chemical Physics Letters* **2013**, *580*, 166–171.

[32] B. Chan, W. L. Yim, *Journal of Chemical Theory and Computation* **2013**, *9*, 1964–
      1970.

[33] M. Mantina, R. Valero, D. G. Truhlar, *Journal of Chemical Physics* **2009**, *131*, 1–6.

[34] Y.-K. Shi, Z. H. Li, K.-N. Fan, *The journal of physical chemistry. A* **2010**, *114*,
      10297–10308.

[35] D. A. Götz, R. Schäfer, P. Schwerdtfeger, *Journal of Computational Chemistry*
      2013, *34*, 1975–1981.

[36] M. Mahmoodinia, P.-O. Åstrand, D. Chen, *The Journal of Physical Chemistry C*
      2015, *119*, 24425–24438.

[37] G. A. Bishea, M. D. Morse, *The Journal of Chemical Physics* **1991**, *95*, 5646–5659.

[38] A. James, P. Kowalczyk, B. Simard, J. Pinegar, M. Morse, *Journal of Molecular Spectroscopy* **1994**, *168*, 248–257.

[39] S. van Gisbergen, J. Snijders, E. Baerends, *Computer Physics Communications* **1999**, *118*, 119–138.

[40] J. Li, X. Li, H.-J. Zhai, L.-S. Wang, *Science* **2003**, *299*, 864.

[41] P. Gruene, D. M. Rayner, B. Redlich, A. F. G. van der Meer, J. T. Lyon, G. Meijer, A. Fielicke, *Science (New York N.Y.)* **2008**, *321*, 674–676.

[42] G. H. Aylward, T. J. V. Findlay, *SI Chemical Data, 6th Edition*, John Wiley & Sons, **2008**.

[43] D. Wales, J. P. K. Doye, *Journal of Physical Chemistry A* **1997**, *101*, 5111–5116.

[44] G. Frenking, C. Loschen, A. Krapp, S. Fau, S. H. Strauss, *Journal of computational chemistry* **2007**, *28*, 117–126.

[45] H. Jacobsen, A. Bérces, D. P. Swerhone, T. Ziegler, *Computer Physics Communications* **1997**, *100*, 263–276.

[46] A Berces, R. M. Dickson, L. Y. Fan, H Jacobsen, D Swerhone, T Ziegler, *Computer Physics Communications* **1997**, *100*, 247–262.

[47] S. K. Wolff, *International Journal of Quantum Chemistry* **2005**, *104*, 645–659.

A Regular tetrahedron Au$_{20}$ in an electric field

The full solution of the set of coupled equations (45)-(52) for the atomic charges of an Au$_{20}$ cluster with a regular tetrahedron structure in a homogeneous external electric field is:

$$
\begin{aligned}
q_{v0} = - \Big(& E \left(3\sqrt{6}\eta_e^3\eta_f^2 r^7 + 3\sqrt{6}\eta_e^3\eta_f\eta_v r^7 + 6\sqrt{6}\eta_e^3\eta_f r^6 - 3\sqrt{6}\eta_e^3\eta_v r^6 - 9\sqrt{6}\eta_e^3 r^5 + 9\sqrt{6}\eta_e^2\eta_f^2\eta_v r^7 \right. \\
& - 11\sqrt{6}\eta_e^2\eta_f^2 r^6 - 11\sqrt{6}\eta_e^2\eta_f\eta_v r^6 - 41\sqrt{6}\eta_e^2\eta_f r^5 - 8\sqrt{6}\eta_e^2\eta_v r^5 + 12\sqrt{6}\eta_e^2 r^4 \\
& - 6\sqrt{6}\eta_e\eta_f^2\eta_v r^6 + 6\sqrt{6}\eta_e\eta_f^2 r^5 - 24\sqrt{6}\eta_e\eta_f\eta_v r^5 + 52\sqrt{6}\eta_e\eta_f r^4 + 4\sqrt{6}\eta_e\eta_v r^4 \\
& + 108\sqrt{6}\eta_e r^3 + 12\sqrt{6}\eta_f\eta_v r^4 - 12\sqrt{6}\eta_f r^3 - 48\sqrt{6}r^2 \left.\right) - 12\eta_e^3\eta_f\eta_v r^6\xi_f + 12\eta_e^3\eta_f\eta_v r^6\xi_v \\
& + 12\eta_e^3\eta_v r^5\xi_f - 12\eta_e^3\eta_v r^5\xi_v - 36\eta_e^2\eta_f^2\eta_v r^6\xi_e + 36\eta_e^2\eta_f^2\eta_v r^6\xi_v - 36\eta_e^2\eta_f\eta_v r^5\xi_e \\
& + 60\eta_e^2\eta_f\eta_v r^5\xi_f - 24\eta_e^2\eta_f\eta_v r^5\xi_v + 36\eta_e^2\eta_f r^4\xi_f - 36\eta_e^2\eta_f r^4\xi_v + 72\eta_e^2\eta_v r^4\xi_e - 12\eta_e^2\eta_v r^4\xi_f \\
& - 60\eta_e^2\eta_v r^4\xi_v - 36\eta_e^2 r^3\xi_f + 36\eta_e^2 r^3\xi_v - 36\eta_e\eta_f^2\eta_v r^5\xi_e + 36\eta_e\eta_f^2\eta_v r^5\xi_v + 108\eta_e\eta_f^2 r^4\xi_e \\
& - 108\eta_e\eta_f^2 r^4\xi_v + 108\eta_e\eta_f\eta_v r^4\xi_e + 96\eta_e\eta_f\eta_v r^4\xi_f - 204\eta_e\eta_f\eta_v r^4\xi_v + 108\eta_e\eta_f r^3\xi_e \\
& - 240\eta_e\eta_f r^3\xi_f + 132\eta_e\eta_f r^3\xi_v + 360\eta_e\eta_v r^3\xi_e - 384\eta_e\eta_v r^3\xi_f + 24\eta_e\eta_v r^3\xi_v - 216\eta_e r^2\xi_e \\
& + 144\eta_e r^2\xi_f + 72\eta_e r^2\xi_v + 72\eta_f^2\eta_v r^4\xi_e - 72\eta_f^2\eta_v r^4\xi_v - 72\eta_f^2 r^3\xi_e + 72\eta_f^2 r^3\xi_v + 72\eta_f\eta_v r^3\xi_e \\
& - 144\eta_f\eta_v r^3\xi_f + 72\eta_f\eta_v r^3\xi_v - 360\eta_f r^2\xi_e + 144\eta_f r^2\xi_f + 216\eta_f r^2\xi_v - 144\eta_v r^2\xi_e \\
& + 144\eta_v r^2\xi_f - 432r\xi_e + 432r\xi_f \Big) \Big/ \Big(12\eta_e^3\eta_f^2\eta_v r^6 + 12\eta_e^3\eta_f\eta_v^2 r^6 + 24\eta_e^3\eta_f\eta_v r^5 - 12\eta_e^3\eta_v^2 r^5 \\
& - 36\eta_e^3\eta_v r^4 + 36\eta_e^2\eta_f^2\eta_v^2 r^6 - 24\eta_e^2\eta_f^2\eta_v r^5 - 36\eta_e^2\eta_f^2 r^4 - 24\eta_e^2\eta_f\eta_v^2 r^5 - 168\eta_e^2\eta_f\eta_v r^4 \\
& - 72\eta_e^2\eta_f r^3 - 60\eta_e^2\eta_v^2 r^4 + 108\eta_e^2 r^2 + 36\eta_e\eta_f^2\eta_v^2 r^5 - 168\eta_e\eta_f^2\eta_v r^4 + 132\eta_e\eta_f^2 r^3 \\
& - 204\eta_e\eta_f\eta_v^2 r^4 + 120\eta_e\eta_f\eta_v r^3 + 468\eta_e\eta_f r^2 + 24\eta_e\eta_v^2 r^3 + 864\eta_e\eta_v r^2 - 216\eta_e r \\
& - 72\eta_f^2\eta_v^2 r^4 + 144\eta_f^2\eta_v r^3 - 72\eta_f^2 r^2 + 72\eta_f\eta_v^2 r^3 + 432\eta_f\eta_v r^2 - 504\eta_f r - 288\eta_v r - 864 \Big)
\end{aligned}
$$

$$q_{e1} = \Big(E \big(\sqrt{6}\eta_e^2\eta_f^2\eta_v r^7 + 3\sqrt{6}\eta_e^2\eta_f^2 r^6 + \sqrt{6}\eta_e^2\eta_f\eta_v^2 r^7 + 3\sqrt{6}\eta_e^2\eta_f\eta_v r^6 + 6\sqrt{6}\eta_e^2\eta_f r^5$$
$$- 3\sqrt{6}\eta_e^2\eta_v^2 r^6 - 12\sqrt{6}\eta_e^2\eta_v r^5 - 9\sqrt{6}\eta_e^2 r^4 + 3\sqrt{6}\eta_e\eta_f^2\eta_v^2 r^7 + 8\sqrt{6}\eta_e\eta_f^2\eta_v r^6$$
$$- 11\sqrt{6}\eta_e\eta_f^2 r^5 - 7\sqrt{6}\eta_e\eta_f\eta_v^2 r^6 - 6\sqrt{6}\eta_e\eta_f\eta_v r^5 - 47\sqrt{6}\eta_e\eta_f r^4 + 2\sqrt{6}\eta_e\eta_v^2 r^5$$
$$+ 28\sqrt{6}\eta_e\eta_v r^4 - 6\sqrt{6}\eta_e r^3 + 6\sqrt{6}\eta_f^2\eta_v^2 r^6 - 12\sqrt{6}\eta_f^2\eta_v r^5 + 6\sqrt{6}\eta_f^2 r^4 + 6\sqrt{6}\eta_f\eta_v^2 r^5$$
$$- 72\sqrt{6}\eta_f\eta_v r^4 + 66\sqrt{6}\eta_f r^3 - 24\sqrt{6}\eta_v r^3 + 168\sqrt{6} r^2 \big) - 12\eta_e^2\eta_f^2\eta_v r^6\xi_e + 12\eta_e^2\eta_f^2\eta_v r^6\xi_v$$
$$- 12\eta_e^2\eta_f\eta_v^2 r^6\xi_e + 12\eta_e^2\eta_f\eta_v^2 r^6\xi_f - 24\eta_e^2\eta_f\eta_v r^5\xi_e + 12\eta_e^2\eta_f\eta_v r^5\xi_f + 12\eta_e^2\eta_f\eta_v r^5\xi_v$$
$$+ 12\eta_e^2\eta_v^2 r^5\xi_e - 12\eta_e^2\eta_v^2 r^5\xi_f + 36\eta_e^2\eta_v r^4\xi_e - 12\eta_e^2\eta_v r^4\xi_f - 24\eta_e^2\eta_v r^4\xi_v - 12\eta_e\eta_f^2\eta_v r^5\xi_e$$
$$+ 12\eta_e\eta_f^2\eta_v r^5\xi_v + 36\eta_e\eta_f^2 r^4\xi_e - 36\eta_e\eta_f^2 r^4\xi_v - 12\eta_e\eta_f\eta_v^2 r^5\xi_e + 12\eta_e\eta_f\eta_v^2 r^5\xi_f$$
$$+ 60\eta_e\eta_f\eta_v r^4\xi_e - 24\eta_e\eta_f\eta_v r^4\xi_f - 36\eta_e\eta_f\eta_v r^4\xi_v + 72\eta_e\eta_f r^3\xi_e - 36\eta_e\eta_f r^3\xi_f$$
$$- 36\eta_e\eta_f r^3\xi_v + 60\eta_e\eta_v^2 r^4\xi_e - 60\eta_e\eta_v^2 r^4\xi_f + 144\eta_e\eta_v r^3\xi_e - 24\eta_e\eta_v r^3\xi_f - 120\eta_e\eta_v r^3\xi_v$$
$$- 108\eta_e r^2\xi_e + 36\eta_e r^2\xi_f + 72\eta_e r^2\xi_v + 24\eta_f^2\eta_v r^4\xi_e - 24\eta_f^2\eta_v r^4\xi_v - 24\eta_f^2 r^3\xi_e + 24\eta_f^2 r^3\xi_v$$
$$+ 24\eta_f\eta_v^2 r^4\xi_e - 24\eta_f\eta_v^2 r^4\xi_f + 24\eta_f\eta_v r^3\xi_e - 24\eta_f\eta_v r^3\xi_v - 144\eta_f r^2\xi_e + 24\eta_f r^2\xi_f$$
$$+ 120\eta_f r^2\xi_v - 24\eta_v^2 r^3\xi_e + 24\eta_v^2 r^3\xi_f - 144\eta_v r^2\xi_e + 96\eta_v r^2\xi_f + 48\eta_v r^2\xi_v - 216 r\xi_e$$
$$+ 72 r\xi_f + 144 r\xi_v \big) \Big/ \big(12\eta_e^3\eta_f^2\eta_v r^6 + 12\eta_e^3\eta_f\eta_v^2 r^6 + 24\eta_e^3\eta_f\eta_v r^5 - 12\eta_e^3\eta_v^2 r^5 - 36\eta_e^3\eta_v r^4$$
$$+ 36\eta_e^2\eta_f^2\eta_v^2 r^6 - 24\eta_e^2\eta_f^2\eta_v r^5 - 36\eta_e^2\eta_f^2 r^4 - 24\eta_e^2\eta_f\eta_v^2 r^5 - 168\eta_e^2\eta_f\eta_v r^4 - 72\eta_e^2\eta_f r^3$$
$$- 60\eta_e^2\eta_v^2 r^4 + 108\eta_e^2 r^2 + 36\eta_e\eta_f^2\eta_v^2 r^5 - 168\eta_e\eta_f^2\eta_v r^4 + 132\eta_e\eta_f^2 r^3 - 204\eta_e\eta_f\eta_v^2 r^4$$
$$+ 120\eta_e\eta_f\eta_v r^3 + 468\eta_e\eta_f r^2 + 24\eta_e\eta_v^2 r^3 + 864\eta_e\eta_v r^2 - 216\eta_e r - 72\eta_f^2\eta_v^2 r^4$$
$$+ 144\eta_f^2\eta_v r^3 - 72\eta_f^2 r^2 + 72\eta_f\eta_v^2 r^3 + 432\eta_f\eta_v r^2 - 504\eta_f r - 288\eta_v r - 864 \big)$$

$$q_{f1} = \Big(E \big(\sqrt{6}\eta_e^3\eta_f\eta_v r^7 + \sqrt{6}\eta_e^3\eta_v^2 r^7 + 3\sqrt{6}\eta_e^3\eta_v r^6 + 3\sqrt{6}\eta_e^2\eta_f\eta_v^2 r^7 - 8\sqrt{6}\eta_e^2\eta_f\eta_v r^6 + 3\sqrt{6}\eta_e^2\eta_f r^5$$
$$- 5\sqrt{6}\eta_e^2\eta_v^2 r^6 - 24\sqrt{6}\eta_e^2\eta_v r^5 + 9\sqrt{6}\eta_e^2 r^4 - 15\sqrt{6}\eta_e\eta_f\eta_v^2 r^6 + 26\sqrt{6}\eta_e\eta_f\eta_v r^5$$
$$- 11\sqrt{6}\eta_e\eta_f r^4 + 2\sqrt{6}\eta_e\eta_v^2 r^5 + 64\sqrt{6}\eta_e\eta_v r^4 - 42\sqrt{6}\eta_e r^3 + 6\sqrt{6}\eta_f\eta_v^2 r^5 - 12\sqrt{6}\eta_f\eta_v r^4$$
$$+ 6\sqrt{6}\eta_f r^3 - 24\sqrt{6}\eta_v r^3 + 24\sqrt{6} r^2 \big) - 12\eta_e^3\eta_f\eta_v r^6\xi_f + 12\eta_e^3\eta_f\eta_v r^6\xi_v + 12\eta_e^3\eta_v r^5\xi_f$$
$$- 12\eta_e^3\eta_v r^5\xi_v + 36\eta_e^2\eta_f\eta_v^2 r^6\xi_e - 36\eta_e^2\eta_f\eta_v^2 r^6\xi_f + 36\eta_e^2\eta_f\eta_v r^5\xi_e + 24\eta_e^2\eta_f\eta_v r^5\xi_f$$
$$- 60\eta_e^2\eta_f\eta_v r^5\xi_v + 36\eta_e^2\eta_f r^4\xi_f - 36\eta_e^2\eta_f r^4\xi_v - 36\eta_e^2\eta_v^2 r^5\xi_e + 36\eta_e^2\eta_v^2 r^5\xi_f - 36\eta_e^2\eta_v r^4\xi_e$$
$$+ 24\eta_e^2\eta_v r^4\xi_f + 12\eta_e^2\eta_v r^4\xi_v - 36\eta_e^2 r^3\xi_f + 36\eta_e^2 r^3\xi_v + 36\eta_e\eta_f\eta_v^2 r^5\xi_e - 36\eta_e\eta_f\eta_v^2 r^5\xi_f$$
$$- 72\eta_e\eta_f\eta_v r^4\xi_e + 168\eta_e\eta_f\eta_v r^4\xi_f - 96\eta_e\eta_f\eta_v r^4\xi_v - 108\eta_e\eta_f r^3\xi_e - 132\eta_e\eta_f r^3\xi_f$$
$$+ 240\eta_e\eta_f r^3\xi_v - 180\eta_e\eta_v^2 r^4\xi_e + 180\eta_e\eta_v^2 r^4\xi_f - 72\eta_e\eta_v r^3\xi_e - 312\eta_e\eta_v r^3\xi_f$$
$$+ 384\eta_e\eta_v r^3\xi_v + 108\eta_e r^2\xi_e + 36\eta_e r^2\xi_f - 144\eta_e r^2\xi_v - 72\eta_f\eta_v^2 r^4\xi_e + 72\eta_f\eta_v^2 r^4\xi_f$$
$$- 144\eta_f\eta_v r^3\xi_f + 144\eta_f\eta_v r^3\xi_v + 72\eta_f r^2\xi_e + 72\eta_f r^2\xi_f - 144\eta_f r^2\xi_v + 72\eta_v^2 r^3\xi_e$$
$$- 72\eta_v^2 r^3\xi_f + 288\eta_v r^2\xi_e - 144\eta_v r^2\xi_f - 144\eta_v r^2\xi_v + 216 r\xi_e + 216 r\xi_f$$
$$- 432 r\xi_v \big) \Big/ \big(12\eta_e^3\eta_f^2\eta_v r^6 + 12\eta_e^3\eta_f\eta_v^2 r^6 + 24\eta_e^3\eta_f\eta_v r^5 - 12\eta_e^3\eta_v^2 r^5 - 36\eta_e^3\eta_v r^4$$
$$+ 36\eta_e^2\eta_f^2\eta_v^2 r^6 - 24\eta_e^2\eta_f^2\eta_v r^5 - 36\eta_e^2\eta_f^2 r^4 - 24\eta_e^2\eta_f\eta_v^2 r^5 - 168\eta_e^2\eta_f\eta_v r^4 - 72\eta_e^2\eta_f r^3$$
$$- 60\eta_e^2\eta_v^2 r^4 + 108\eta_e^2 r^2 + 36\eta_e\eta_f^2\eta_v^2 r^5 - 168\eta_e\eta_f^2\eta_v r^4 + 132\eta_e\eta_f^2 r^3 - 204\eta_e\eta_f\eta_v^2 r^4$$
$$+ 120\eta_e\eta_f\eta_v r^3 + 468\eta_e\eta_f r^2 + 24\eta_e\eta_v^2 r^3 + 864\eta_e\eta_v r^2 - 216\eta_e r - 72\eta_f^2\eta_v^2 r^4$$
$$+ 144\eta_f^2\eta_v r^3 - 72\eta_f^2 r^2 + 72\eta_f\eta_v^2 r^3 + 432\eta_f\eta_v r^2 - 504\eta_f r - 288\eta_v r - 864 \big)$$

$$q_{f0} = -\Big(E\left(\sqrt{6}\eta_e^3\eta_f\eta_v r^7 + \sqrt{6}\eta_e^3\eta_v^2 r^7 + 3\sqrt{6}\eta_e^3\eta_v r^6 + 3\sqrt{6}\eta_e^2\eta_f\eta_v^2 r^7 - 8\sqrt{6}\eta_e^2\eta_f\eta_v r^6\right.$$
$$+ 3\sqrt{6}\eta_e^2\eta_f r^5 - 5\sqrt{6}\eta_e^2\eta_v^2 r^6 - 24\sqrt{6}\eta_e^2\eta_v r^5 + 9\sqrt{6}\eta_e^2 r^4 - 15\sqrt{6}\eta_e\eta_f\eta_v^2 r^6$$
$$+ 26\sqrt{6}\eta_e\eta_f\eta_v r^5 - 11\sqrt{6}\eta_e\eta_f r^4 + 2\sqrt{6}\eta_e\eta_v^2 r^5 + 64\sqrt{6}\eta_e\eta_v r^4 - 42\sqrt{6}\eta_e r^3 + 6\sqrt{6}\eta_f\eta_v^2 r^5$$
$$\left. - 12\sqrt{6}\eta_f\eta_v r^4 + 6\sqrt{6}\eta_f r^3 - 24\sqrt{6}\eta_v r^3 + 24\sqrt{6}r^2\right) + 4\eta_e^3\eta_f\eta_v r^6\xi_f - 4\eta_e^3\eta_f\eta_v r^6\xi_v$$
$$- 4\eta_e^3\eta_v r^5\xi_f + 4\eta_e^3\eta_v r^5\xi_v - 12\eta_e^2\eta_f\eta_v^2 r^6\xi_e + 12\eta_e^2\eta_f\eta_v^2 r^6\xi_f - 12\eta_e^2\eta_f\eta_v r^5\xi_e$$
$$- 8\eta_e^2\eta_f\eta_v r^5\xi_f + 20\eta_e^2\eta_f\eta_v r^5\xi_v - 12\eta_e^2\eta_f r^4\xi_f + 12\eta_e^2\eta_f r^4\xi_v + 12\eta_e^2\eta_v^2 r^5\xi_e - 12\eta_e^2\eta_v^2 r^5\xi_f$$
$$+ 12\eta_e^2\eta_v r^4\xi_e - 8\eta_e^2\eta_v r^4\xi_f - 4\eta_e^2\eta_v r^4\xi_v + 12\eta_e^2 r^3\xi_f - 12\eta_e^2 r^3\xi_v - 12\eta_e\eta_f\eta_v^2 r^5\xi_e$$
$$+ 12\eta_e\eta_f\eta_v^2 r^5\xi_f + 24\eta_e\eta_f\eta_v r^4\xi_e - 56\eta_e\eta_f\eta_v r^4\xi_f + 32\eta_e\eta_f\eta_v r^4\xi_v + 36\eta_e\eta_f r^3\xi_e$$
$$+ 44\eta_e\eta_f r^3\xi_f - 80\eta_e\eta_f r^3\xi_v + 60\eta_e\eta_v^2 r^4\xi_e - 60\eta_e\eta_v^2 r^4\xi_f + 24\eta_e\eta_v r^3\xi_e + 104\eta_e\eta_v r^3\xi_f$$
$$- 128\eta_e\eta_v r^3\xi_v - 36\eta_e r^2\xi_e - 12\eta_e r^2\xi_f + 48\eta_e r^2\xi_v + 24\eta_f\eta_v^2 r^4\xi_e - 24\eta_f\eta_v^2 r^4\xi_f$$
$$+ 48\eta_f\eta_v r^3\xi_f - 48\eta_f\eta_v r^3\xi_v - 24\eta_f r^2\xi_e - 24\eta_f r^2\xi_f + 48\eta_f r^2\xi_v - 24\eta_v^2 r^3\xi_e + 24\eta_v^2 r^3\xi_f$$
$$- 96\eta_v r^2\xi_e + 48\eta_v r^2\xi_f + 48\eta_v r^2\xi_v - 72r\xi_e - 72r\xi_f + 144r\xi_v\Big) \Big/ \Big(4\eta_e^3\eta_f^2\eta_v r^6 + 4\eta_e^3\eta_f\eta_v^2 r^6$$
$$+ 8\eta_e^3\eta_f\eta_v r^5 - 4\eta_e^3\eta_v^2 r^5 - 12\eta_e^3\eta_v r^4 + 12\eta_e^2\eta_f^2\eta_v^2 r^6 - 8\eta_e^2\eta_f^2\eta_v r^5 - 12\eta_e^2\eta_f^2 r^4 - 8\eta_e^2\eta_f\eta_v^2 r^5$$
$$- 56\eta_e^2\eta_f\eta_v r^4 - 24\eta_e^2\eta_f r^3 - 20\eta_e^2\eta_v^2 r^4 + 36\eta_e^2 r^2 + 12\eta_e\eta_f^2\eta_v^2 r^5 - 56\eta_e\eta_f^2\eta_v r^4$$
$$+ 44\eta_e\eta_f^2 r^3 - 68\eta_e\eta_f\eta_v^2 r^4 + 40\eta_e\eta_f\eta_v r^3 + 156\eta_e\eta_f r^2 + 8\eta_e\eta_v^2 r^3 + 288\eta_e\eta_v r^2 - 72\eta_e r$$
$$- 24\eta_f^2\eta_v^2 r^4 + 48\eta_f^2\eta_v r^3 - 24\eta_f^2 r^2 + 24\eta_f\eta_v^2 r^3 + 144\eta_f\eta_v r^2 - 168\eta_f r - 96\eta_v r - 288\Big)$$

$$\mu = \frac{Er}{4}\sqrt{6} - \xi_v - \frac{1}{\eta_e\eta_f r^2 + \eta_e\eta_v r^2 + 3\eta_e r + 3\eta_f\eta_v r^2 - 3\eta_f r - 12}\Big(\eta_e\eta_v r^2\xi_f - \eta_e\eta_v r^2\xi_v$$
$$+ 3\eta_f\eta_v r^2\xi_e - 3\eta_f\eta_v r^2\xi_v - 3\eta_f r\xi_e + 3\eta_f r\xi_v + 3\eta_v r\xi_e - 3\eta_v r\xi_f - 9\xi_e + 3\xi_f + 6\xi_v\Big)$$

$$q_{v3} = \Big(E\left(3\sqrt{6}\eta_e^3\eta_f^2 r^7 + 3\sqrt{6}\eta_e^3\eta_f\eta_v r^7 + 6\sqrt{6}\eta_e^3\eta_f r^6 - 3\sqrt{6}\eta_e^3\eta_v r^6 - 9\sqrt{6}\eta_e^3 r^5 + 9\sqrt{6}\eta_e^2\eta_f^2\eta_v r^7\right.$$
$$- 11\sqrt{6}\eta_e^2\eta_f^2 r^6 - 11\sqrt{6}\eta_e^2\eta_f\eta_v r^6 - 41\sqrt{6}\eta_e^2\eta_f r^5 - 8\sqrt{6}\eta_e^2\eta_v r^5 + 12\sqrt{6}\eta_e^2 r^4$$
$$- 6\sqrt{6}\eta_e\eta_f^2\eta_v r^6 + 6\sqrt{6}\eta_e\eta_f^2 r^5 - 24\sqrt{6}\eta_e\eta_f\eta_v r^5 + 52\sqrt{6}\eta_e\eta_f r^4 + 4\sqrt{6}\eta_e\eta_v r^4$$
$$\left. + 108\sqrt{6}\eta_e r^3 + 12\sqrt{6}\eta_f\eta_v r^4 - 12\sqrt{6}\eta_f r^3 - 48\sqrt{6}r^2\right) + 4\eta_e^3\eta_f\eta_v r^6\xi_f - 4\eta_e^3\eta_f\eta_v r^6\xi_v$$
$$- 4\eta_e^3\eta_v r^5\xi_f + 4\eta_e^3\eta_v r^5\xi_v + 12\eta_e^2\eta_f^2\eta_v r^6\xi_e - 12\eta_e^2\eta_f^2\eta_v r^6\xi_v + 12\eta_e^2\eta_f\eta_v r^5\xi_e$$
$$- 20\eta_e^2\eta_f\eta_v r^5\xi_f + 8\eta_e^2\eta_f\eta_v r^5\xi_v - 12\eta_e^2\eta_f r^4\xi_f + 12\eta_e^2\eta_f r^4\xi_v - 24\eta_e^2\eta_v r^4\xi_e + 4\eta_e^2\eta_v r^4\xi_f$$
$$+ 20\eta_e^2\eta_v r^4\xi_v + 12\eta_e^2 r^3\xi_f - 12\eta_e^2 r^3\xi_v + 12\eta_e\eta_f^2\eta_v r^5\xi_e - 12\eta_e\eta_f^2\eta_v r^5\xi_v - 36\eta_e\eta_f^2 r^4\xi_e$$
$$+ 36\eta_e\eta_f^2 r^4\xi_v - 36\eta_e\eta_f\eta_v r^4\xi_e - 32\eta_e\eta_f\eta_v r^4\xi_f + 68\eta_e\eta_f\eta_v r^4\xi_v - 36\eta_e\eta_f r^3\xi_e$$
$$+ 80\eta_e\eta_f r^3\xi_f - 44\eta_e\eta_f r^3\xi_v - 120\eta_e\eta_v r^3\xi_e + 128\eta_e\eta_v r^3\xi_f - 8\eta_e\eta_v r^3\xi_v + 72\eta_e r^2\xi_e$$
$$- 48\eta_e r^2\xi_f - 24\eta_e r^2\xi_v - 24\eta_f^2\eta_v r^4\xi_e + 24\eta_f^2\eta_v r^4\xi_v + 24\eta_f^2 r^3\xi_e - 24\eta_f^2 r^3\xi_v$$
$$- 24\eta_f\eta_v r^3\xi_e + 48\eta_f\eta_v r^3\xi_f - 24\eta_f\eta_v r^3\xi_v + 120\eta_f r^2\xi_e - 48\eta_f r^2\xi_f - 72\eta_f r^2\xi_v$$
$$+ 48\eta_v r^2\xi_e - 48\eta_v r^2\xi_f + 144r\xi_e - 144r\xi_f\Big) \Big/ \Big(4\eta_e^3\eta_f^2\eta_v r^6 + 4\eta_e^3\eta_f\eta_v^2 r^6 + 8\eta_e^3\eta_f\eta_v r^5$$
$$- 4\eta_e^3\eta_v^2 r^5 - 12\eta_e^3\eta_v r^4 + 12\eta_e^2\eta_f^2\eta_v^2 r^6 - 8\eta_e^2\eta_f^2\eta_v r^5 - 12\eta_e^2\eta_f^2 r^4 - 8\eta_e^2\eta_f\eta_v^2 r^5$$
$$- 56\eta_e^2\eta_f\eta_v r^4 - 24\eta_e^2\eta_f r^3 - 20\eta_e^2\eta_v^2 r^4 + 36\eta_e^2 r^2 + 12\eta_e\eta_f^2\eta_v^2 r^5 - 56\eta_e\eta_f^2\eta_v r^4$$
$$+ 44\eta_e\eta_f^2 r^3 - 68\eta_e\eta_f\eta_v^2 r^4 + 40\eta_e\eta_f\eta_v r^3 + 156\eta_e\eta_f r^2 + 8\eta_e\eta_v^2 r^3 + 288\eta_e\eta_v r^2 - 72\eta_e r$$
$$- 24\eta_f^2\eta_v^2 r^4 + 48\eta_f^2\eta_v r^3 - 24\eta_f^2 r^2 + 24\eta_f\eta_v^2 r^3 + 144\eta_f\eta_v r^2 - 168\eta_f r - 96\eta_v r - 288\Big)$$

$$
\begin{aligned}
q_{e2} = &\Big(E \Big(5\sqrt{6}\eta_e^2\eta_f^2\eta_v r^7 - 9\sqrt{6}\eta_e^2\eta_f^2 r^6 + 5\sqrt{6}\eta_e^2\eta_f\eta_v^2 r^7 - \sqrt{6}\eta_e^2\eta_f\eta_v r^6 - 18\sqrt{6}\eta_e^2\eta_f r^5 \\
&\quad - 7\sqrt{6}\eta_e^2\eta_v^2 r^6 - 12\sqrt{6}\eta_e^2\eta_v r^5 + 27\sqrt{6}\eta_e^2 r^4 + 15\sqrt{6}\eta_e\eta_f^2\eta_v^2 r^7 - 48\sqrt{6}\eta_e\eta_f^2\eta_v r^6 \\
&\quad + 33\sqrt{6}\eta_e\eta_f^2 r^5 - 27\sqrt{6}\eta_e\eta_f\eta_v^2 r^6 - 22\sqrt{6}\eta_e\eta_f\eta_v r^5 + 117\sqrt{6}\eta_e\eta_f r^4 + 2\sqrt{6}\eta_e\eta_v^2 r^5 \\
&\quad + 108\sqrt{6}\eta_e\eta_v r^4 - 54\sqrt{6}\eta_e r^3 - 18\sqrt{6}\eta_f^2\eta_v^2 r^6 + 36\sqrt{6}\eta_f^2\eta_v r^5 - 18\sqrt{6}\eta_f^2 r^4 + 6\sqrt{6}\eta_f\eta_v^2 r^5 \\
&\quad + 120\sqrt{6}\eta_f\eta_v r^4 - 126\sqrt{6}\eta_f r^3 - 24\sqrt{6}\eta_v r^3 - 216\sqrt{6}r^2 \Big) - 12\eta_e^2\eta_f^2\eta_v r^6\xi_e + 12\eta_e^2\eta_f^2\eta_v r^6\xi_v \\
&\quad - 12\eta_e^2\eta_f\eta_v^2 r^6\xi_e + 12\eta_e^2\eta_f\eta_v^2 r^6\xi_f - 24\eta_e^2\eta_f\eta_v r^5\xi_e + 12\eta_e^2\eta_f\eta_v r^5\xi_f + 12\eta_e^2\eta_f\eta_v r^5\xi_v \\
&\quad + 12\eta_e^2\eta_v^2 r^5\xi_e - 12\eta_e^2\eta_v^2 r^5\xi_f + 36\eta_e^2\eta_v r^4\xi_e - 12\eta_e^2\eta_v r^4\xi_f - 24\eta_e^2\eta_v r^4\xi_v - 12\eta_e\eta_f^2\eta_v r^5\xi_e \\
&\quad + 12\eta_e\eta_f^2\eta_v r^5\xi_v + 36\eta_e\eta_f^2 r^4\xi_e - 36\eta_e\eta_f^2 r^4\xi_v - 12\eta_e\eta_f\eta_v^2 r^5\xi_e + 12\eta_e\eta_f\eta_v^2 r^5\xi_f \\
&\quad + 60\eta_e\eta_f\eta_v r^4\xi_e - 24\eta_e\eta_f\eta_v r^4\xi_f - 36\eta_e\eta_f\eta_v r^4\xi_v + 72\eta_e\eta_f r^3\xi_e - 36\eta_e\eta_f r^3\xi_f \\
&\quad - 36\eta_e\eta_f r^3\xi_v + 60\eta_e\eta_v^2 r^4\xi_e - 60\eta_e\eta_v^2 r^4\xi_f + 144\eta_e\eta_v r^3\xi_e - 24\eta_e\eta_v r^3\xi_f - 120\eta_e\eta_v r^3\xi_v \\
&\quad - 108\eta_e r^2\xi_e + 36\eta_e r^2\xi_f + 72\eta_e r^2\xi_v + 24\eta_f^2\eta_v r^4\xi_e - 24\eta_f^2\eta_v r^4\xi_v - 24\eta_f^2 r^3\xi_e + 24\eta_f^2 r^3\xi_v \\
&\quad + 24\eta_f\eta_v^2 r^4\xi_e - 24\eta_f\eta_v^2 r^4\xi_f + 24\eta_f\eta_v r^3\xi_e - 24\eta_f\eta_v r^3\xi_v - 144\eta_f r^2\xi_e + 24\eta_f r^2\xi_f \\
&\quad + 120\eta_f r^2\xi_v - 24\eta_v^2 r^3\xi_e + 24\eta_v^2 r^3\xi_f - 144\eta_v r^2\xi_e + 96\eta_v r^2\xi_f + 48\eta_v r^2\xi_v - 216r\xi_e \\
&\quad + 72r\xi_f + 144r\xi_v \Big) \Big/ \Big(12\eta_e^3\eta_f^2\eta_v r^6 + 12\eta_e^3\eta_f\eta_v^2 r^6 + 24\eta_e^3\eta_f\eta_v r^5 - 12\eta_e^3\eta_v^2 r^5 - 36\eta_e^3\eta_v r^4 \\
&\quad + 36\eta_e^2\eta_f^2\eta_v^2 r^6 - 24\eta_e^2\eta_f^2\eta_v r^5 - 36\eta_e^2\eta_f^2 r^4 - 24\eta_e^2\eta_f\eta_v^2 r^5 - 168\eta_e^2\eta_f\eta_v r^4 - 72\eta_e^2\eta_f r^3 \\
&\quad - 60\eta_e^2\eta_v^2 r^4 + 108\eta_e^2 r^2 + 36\eta_e\eta_f^2\eta_v^2 r^5 - 168\eta_e\eta_f^2\eta_v r^4 + 132\eta_e\eta_f^2 r^3 - 204\eta_e\eta_f\eta_v^2 r^4 \\
&\quad + 120\eta_e\eta_f\eta_v r^3 + 468\eta_e\eta_f r^2 + 24\eta_e\eta_v^2 r^3 + 864\eta_e\eta_v r^2 - 216\eta_e r - 72\eta_f^2\eta_v^2 r^4 \\
&\quad + 144\eta_f^2\eta_v r^3 - 72\eta_f^2 r^2 + 72\eta_f\eta_v^2 r^3 + 432\eta_f\eta_v r^2 - 504\eta_f r - 288\eta_v r - 864 \Big)
\end{aligned}
$$

$$
\begin{aligned}
q_{e0} = &-\Big(E \Big(3\sqrt{6}\eta_e^2\eta_f^2\eta_v r^7 - 3\sqrt{6}\eta_e^2\eta_f^2 r^6 + 3\sqrt{6}\eta_e^2\eta_f\eta_v^2 r^7 + \sqrt{6}\eta_e^2\eta_f\eta_v r^6 - 6\sqrt{6}\eta_e^2\eta_f r^5 \\
&\quad - 5\sqrt{6}\eta_e^2\eta_v^2 r^6 - 12\sqrt{6}\eta_e^2\eta_v r^5 + 9\sqrt{6}\eta_e^2 r^4 + 9\sqrt{6}\eta_e\eta_f^2\eta_v^2 r^7 - 20\sqrt{6}\eta_e\eta_f^2\eta_v r^6 \\
&\quad + 11\sqrt{6}\eta_e\eta_f^2 r^5 - 17\sqrt{6}\eta_e\eta_f\eta_v^2 r^6 - 14\sqrt{6}\eta_e\eta_f\eta_v r^5 + 35\sqrt{6}\eta_e\eta_f r^4 + 2\sqrt{6}\eta_e\eta_v^2 r^5 \\
&\quad + 68\sqrt{6}\eta_e\eta_v r^4 - 30\sqrt{6}\eta_e r^3 - 6\sqrt{6}\eta_f^2\eta_v^2 r^6 + 12\sqrt{6}\eta_f^2\eta_v r^5 - 6\sqrt{6}\eta_f^2 r^4 + 6\sqrt{6}\eta_f\eta_v^2 r^5 \\
&\quad + 24\sqrt{6}\eta_f\eta_v r^4 - 30\sqrt{6}\eta_f r^3 - 24\sqrt{6}\eta_v r^3 - 24\sqrt{6}r^2 \Big) + 12\eta_e^2\eta_f^2\eta_v r^6\xi_e - 12\eta_e^2\eta_f^2\eta_v r^6\xi_v \\
&\quad + 12\eta_e^2\eta_f\eta_v^2 r^6\xi_e - 12\eta_e^2\eta_f\eta_v^2 r^6\xi_f + 24\eta_e^2\eta_f\eta_v r^5\xi_e - 12\eta_e^2\eta_f\eta_v r^5\xi_f - 12\eta_e^2\eta_f\eta_v r^5\xi_v \\
&\quad - 12\eta_e^2\eta_v^2 r^5\xi_e + 12\eta_e^2\eta_v^2 r^5\xi_f - 36\eta_e^2\eta_v r^4\xi_e + 12\eta_e^2\eta_v r^4\xi_f + 24\eta_e^2\eta_v r^4\xi_v + 12\eta_e\eta_f^2\eta_v r^5\xi_e \\
&\quad - 12\eta_e\eta_f^2\eta_v r^5\xi_v - 36\eta_e\eta_f^2 r^4\xi_e + 36\eta_e\eta_f^2 r^4\xi_v + 12\eta_e\eta_f\eta_v^2 r^5\xi_e - 12\eta_e\eta_f\eta_v^2 r^5\xi_f \\
&\quad - 60\eta_e\eta_f\eta_v r^4\xi_e + 24\eta_e\eta_f\eta_v r^4\xi_f + 36\eta_e\eta_f\eta_v r^4\xi_v - 72\eta_e\eta_f r^3\xi_e + 36\eta_e\eta_f r^3\xi_f \\
&\quad + 36\eta_e\eta_f r^3\xi_v - 60\eta_e\eta_v^2 r^4\xi_e + 60\eta_e\eta_v^2 r^4\xi_f - 144\eta_e\eta_v r^3\xi_e + 24\eta_e\eta_v r^3\xi_f + 120\eta_e\eta_v r^3\xi_v \\
&\quad + 108\eta_e r^2\xi_e - 36\eta_e r^2\xi_f - 72\eta_e r^2\xi_v - 24\eta_f^2\eta_v r^4\xi_e + 24\eta_f^2\eta_v r^4\xi_v + 24\eta_f^2 r^3\xi_e - 24\eta_f^2 r^3\xi_v \\
&\quad - 24\eta_f\eta_v^2 r^4\xi_e + 24\eta_f\eta_v^2 r^4\xi_f - 24\eta_f\eta_v r^3\xi_e + 24\eta_f\eta_v r^3\xi_v + 144\eta_f r^2\xi_e - 24\eta_f r^2\xi_f \\
&\quad - 120\eta_f r^2\xi_v + 24\eta_v^2 r^3\xi_e - 24\eta_v^2 r^3\xi_f + 144\eta_v r^2\xi_e - 96\eta_v r^2\xi_f - 48\eta_v r^2\xi_v + 216r\xi_e \\
&\quad - 72r\xi_f - 144r\xi_v \Big) \Big/ \Big(12\eta_e^3\eta_f^2\eta_v r^6 + 12\eta_e^3\eta_f\eta_v^2 r^6 + 24\eta_e^3\eta_f\eta_v r^5 - 12\eta_e^3\eta_v^2 r^5 - 36\eta_e^3\eta_v r^4 \\
&\quad + 36\eta_e^2\eta_f^2\eta_v^2 r^6 - 24\eta_e^2\eta_f^2\eta_v r^5 - 36\eta_e^2\eta_f^2 r^4 - 24\eta_e^2\eta_f\eta_v^2 r^5 - 168\eta_e^2\eta_f\eta_v r^4 - 72\eta_e^2\eta_f r^3 \\
&\quad - 60\eta_e^2\eta_v^2 r^4 + 108\eta_e^2 r^2 + 36\eta_e\eta_f^2\eta_v^2 r^5 - 168\eta_e\eta_f^2\eta_v r^4 + 132\eta_e\eta_f^2 r^3 - 204\eta_e\eta_f\eta_v^2 r^4 \\
&\quad + 120\eta_e\eta_f\eta_v r^3 + 468\eta_e\eta_f r^2 + 24\eta_e\eta_v^2 r^3 + 864\eta_e\eta_v r^2 - 216\eta_e r - 72\eta_f^2\eta_v^2 r^4 \\
&\quad + 144\eta_f^2\eta_v r^3 - 72\eta_f^2 r^2 + 72\eta_f\eta_v^2 r^3 + 432\eta_f\eta_v r^2 - 504\eta_f r - 288\eta_v r - 864 \Big)
\end{aligned}
$$

B Technical details related to ADF input

In this appendix, some technical details regarding the setup of the calculations in ADF are presented. As previously mentioned, ADF 2014.10 [28–30] was used for all calculations. Where no details are given, it may be assumed that the default settings were used. The exchange-correlation functional PBE [18] was used, with Grimme's DFT-D3(BJ) [24] dispersion correction. Scalar-relativistic ZORA [25–27] was used to include relativistic effects. For Au, a TZ2P basis set with a frozen core up to and including the 4d subshell was used. A TZ2P basis set was used for all other elements. All basis sets used were the default ones included in ADF [16], of the kind made for use with ZORA. Unless otherwise stated, neutral charge and singlet spin state was specified. The `DEPENDENCY` keyword was included in the input to check and correct for linear dependencies in the basis. In geometry optimizations, the convergence criteria `converge E=1.0e-5 Grad=1.0e-5 Rad=1.0e-4 Angle=1.0e-2` were specified. For the SCF procedure, the convergence criterion `converge 1.0e-6` was specified. A Becke grid quality *good* (using ADF terminology) was used throughout. The implementation of analytical calculation of the frequencies [45–47] was used for vibration frequency calculations. All localized orbitals were found using a Boys-Foster type localization procedure [14], as implemented in ADF.

The geometry optimization of Au_{58} had a slightly different setup than the other calculations due to slow convergence. The convergence criterion for the geometry optimization was specified as `converge grad=2e-3`. In addition `NUMERICALQUALITY GOOD` was specified, meaning the quality of the fit density is also set to *good* in addition to the Becke grid.

Zero-point vibrational corrections have not been considered in this work.

C Geometries

C.1 Initial cluster geometries

This section contains the cartesian coordinates (in Å) of the initial geometries used as input in the geometry optimizations of Au$_2$, Au$_4$, Au$_{20}$ and Au$_{58}$.

C.1.1 Au$_2$

Element	x[Å]	y[Å]	z[Å]
Au	0.00000	0.00000	1.50000
Au	0.00000	0.00000	-1.50000

C.1.2 Au$_4$

Element	x[Å]	y[Å]	z[Å]
Au	-1.90989	3.15881	0.00000
Au	-3.47253	0.26764	0.00000
Au	-0.17420	0.36809	0.00000
Au	-1.73685	-2.52310	0.00000

C.1.3 Au$_{20}$

Element	x[Å]	y[Å]	z[Å]
Au	2.34210	2.41173	-0.04096
Au	-0.17321	2.96523	-1.57666
Au	-0.19805	3.04010	1.42447
Au	1.14338	4.89567	-0.11233
Au	1.00009	0.44944	1.54257
Au	-1.47220	1.10038	2.81512
Au	-1.59255	1.01942	-0.03846
Au	-1.42523	0.95845	-2.89019
Au	1.02562	0.37245	-1.54680
Au	3.36000	-0.09504	0.02983
Au	-2.84095	-1.19157	-1.34718
Au	-2.86347	-1.12427	1.35774
Au	-2.72342	-0.98844	4.10872
Au	-0.34588	-1.67827	2.89316
Au	1.94639	-2.24644	1.57323
Au	4.23125	-2.71245	0.10261

60

Au	1.97109	-2.32130	-1.42697
Au	-0.29882	-1.82072	-2.81142
Au	-2.65559	-1.19284	-4.09878
Au	-0.43057	-1.84154	0.04230

C.1.4   Au$_{58}$

Element	x[Å]	y[Å]	z[Å]
Au	-0.64560	1.91759	-0.19747
Au	1.65730	1.23624	-0.51258
Au	1.19240	-0.93445	0.70984
Au	-1.31881	-0.44270	0.87302
Au	-0.22118	-2.80711	0.81696
Au	-4.10141	-1.35308	0.01549
Au	-2.63179	-3.85441	-0.16843
Au	2.36328	-3.34051	0.33976
Au	3.55092	-0.55830	-0.28944
Au	-0.67339	-5.19835	-0.22082
Au	2.84367	-5.43145	-2.10338
Au	3.39665	-2.64220	-1.34459
Au	3.61876	1.59545	-2.21842
Au	4.32267	-0.84978	-3.08701
Au	1.02539	2.49717	-2.28995
Au	-1.60290	2.78366	-2.51014
Au	-1.48681	2.33833	-5.63640
Au	0.90652	2.91222	-4.77254
Au	3.67564	1.39489	-4.68471
Au	-2.99131	0.60197	-0.87147
Au	-5.18582	-0.45008	-2.43602
Au	-3.65721	2.25739	-3.52872
Au	-4.47249	-3.16948	-2.40256
Au	-4.28071	-4.73434	-4.33042
Au	-1.87404	-6.37330	-3.10563
Au	0.57886	-6.48370	-3.66207
Au	-0.21335	-6.16757	-6.22873
Au	-2.63486	-6.04126	-5.75308
Au	-0.09095	1.56358	-7.10700
Au	-2.82592	1.43210	-6.68762

```
Au       -1.68335      -0.13937      -7.93142
Au        0.88775      -0.14237      -8.41212
Au        2.08184       1.29082      -6.81891
Au        3.87475      -1.22531      -5.65925
Au        2.42892      -1.90353      -7.56660
Au       -3.52156      -3.84378      -6.55706
Au       -1.40056      -4.46071      -7.40236
Au        1.52878      -4.85551      -7.87768
Au       -2.54452      -2.34723      -8.41288
Au        0.11122      -2.52575      -8.55430
Au       -5.00274       0.10567      -5.04736
Au       -4.00795      -0.98418      -6.76466
Au       -4.80125      -2.40110      -4.70652
Au        2.97463      -4.93193      -5.17951
Au        3.58026      -3.86327      -6.15672
Au        4.42732      -2.90711      -3.62784
Au       -0.95076       0.20895      -2.25497
Au        1.33404      -0.00605      -3.24907
Au       -1.76976      -2.00545      -1.46467
Au        0.53004      -1.74635      -1.57467
Au       -0.78206      -0.29335      -4.90447
Au       -2.64876      -1.19305      -3.83737
Au       -0.33276      -1.88585      -3.52757
Au        2.10824      -2.37035      -3.15197
Au        1.10084      -1.54585      -5.46877
Au       -1.73936      -3.61155      -3.28547
Au       -1.29436      -2.52455      -5.59947
Au        0.51324      -3.82345      -4.26567
```

C.2 Optimized cluster geometries

This section contains the cartesian coordinates (in Å) of the final geometries from the geometry optimizations of Au$_2$, Au$_4$, Au$_{20}$ and Au$_{58}$.

C.2.1 Au$_2$

```
Element     x[Å]         y[Å]         z[Å]
  Au      0.000000     0.000000     1.261508
```

```
Au          0.000000      0.000000     -1.261508
```

C.2.2 Au$_4$

Element	x[Å]	y[Å]	z[Å]
Au	0.000000	2.339864	0.000000
Au	-1.313549	0.000000	0.000000
Au	1.313549	0.000000	0.000000
Au	0.000000	-2.339864	0.000000

C.2.3 Au$_{20}$

Element	x[Å]	y[Å]	z[Å]
Au	2.288637	2.369128	-0.039350
Au	-0.164404	2.908177	-1.537098
Au	-0.189017	2.980537	1.386452
Au	1.124137	4.807103	-0.110388
Au	0.998768	0.448400	1.539756
Au	-1.446181	1.068347	2.759295
Au	-1.592321	1.019795	-0.038744
Au	-1.399557	0.928950	-2.832840
Au	1.024172	0.372030	-1.543201
Au	3.291918	-0.103495	0.029676
Au	-2.779213	-1.164672	-1.328966
Au	-2.801796	-1.098088	1.339225
Au	-2.674555	-0.972785	4.035510
Au	-0.346914	-1.639024	2.835568
Au	1.912994	-2.199970	1.531957
Au	4.157447	-2.662548	0.099902
Au	1.937110	-2.272215	-1.389091
Au	-0.301632	-1.778429	-2.754636
Au	-2.608073	-1.173353	-4.025766
Au	-0.431540	-1.837897	0.042741

C.2.4 Au$_{58}$

Element	x[Å]	y[Å]	z[Å]
Au	-0.822089	2.100944	-0.027072
Au	1.714919	1.254879	0.162373

```
Au        1.251269    -1.109076     1.507425
Au       -1.469215    -0.402253     0.861243
Au       -0.629434    -3.015382     0.880376
Au       -4.021978    -1.570576     0.193373
Au       -2.779298    -4.224882    -0.174924
Au        1.931939    -3.416465    -0.037473
Au        3.388729    -0.924489    -0.400726
Au       -0.150527    -5.128568    -0.822154
Au        2.342129    -5.265326    -2.072376
Au        4.303331    -3.318657    -1.439494
Au        3.497581     1.504031    -1.874569
Au        4.489588    -0.826644    -2.978159
Au        0.987080     2.696338    -2.214806
Au       -1.781818     3.370917    -2.228267
Au       -1.390525     2.967121    -4.880384
Au        1.323210     2.654823    -4.984229
Au        3.854142     1.505643    -4.604480
Au       -3.229544     1.000175    -0.852751
Au       -4.920099    -0.617547    -2.346130
Au       -3.674207     1.840084    -3.511227
Au       -4.636337    -3.352495    -1.957723
Au       -4.518501    -5.263823    -3.994064
Au       -2.368608    -5.907795    -2.280724
Au        0.175776    -6.487153    -3.235119
Au        0.586088    -6.598246    -6.012229
Au       -2.023843    -6.102691    -5.071978
Au       -0.337873     2.211676    -7.381980
Au       -3.090536     1.330428    -6.291441
Au       -1.796704    -0.201074    -8.173340
Au        0.782525     0.196581    -8.936051
Au        2.331728     0.843526    -6.817920
Au        4.199336    -0.993059    -5.751943
Au        2.718382    -1.654252    -8.197038
Au       -3.682824    -4.144885    -6.400750
Au       -1.141610    -4.874517    -7.443435
Au        1.584507    -4.395382    -7.413487
Au       -2.642957    -2.863103    -8.658326
```

```
Au        0.083435   -2.464212   -8.660811
Au       -5.350147    0.222946   -4.977714
Au       -4.065555   -1.322006   -6.878198
Au       -5.150892   -2.545629   -4.571707
Au        2.787016   -5.251392   -4.820818
Au        4.036656   -3.567029   -6.719347
Au        4.724541   -3.326818   -4.135576
Au       -1.018358    0.744896   -2.658308
Au        1.697898    0.141093   -3.567776
Au       -2.054588   -1.834065   -1.584753
Au        0.643923   -1.086585   -1.172026
Au       -0.429881    0.314223   -5.497642
Au       -2.830054   -0.777458   -4.267227
Au       -0.308366   -1.775704   -3.634722
Au        2.175976   -2.687679   -3.106982
Au        1.473665   -1.836141   -5.782926
Au       -2.388798   -3.549328   -3.790689
Au       -1.366177   -2.274820   -6.210573
Au        0.211606   -4.176158   -4.753686
```

D   Au$_{20}$ coordination sites

The following list gives a detailed specification of the point and vector required to describe the different coordination sites on the surface of the Au$_{20}$ cluster studied in this work.

- Atop sites:

  - Atop, vertex (fig. 3.3a): The point is given by the position of one of the vertex atoms. The vector is defined by normalizing a vector from the center of mass of the cluster to the vertex atom.

  - Atop, face (fig. 3.3b): The point is the position of an atom in the center of one of the triangular faces of the cluster. The vector is given by a unit vector pointing from the center of mass of the cluster to the face atom.

  - Atop, edge (fig. 3.3c): The point is the position of one of the edge atoms. Of the closest neighbours of this atom, two are face atoms, and two are edge atoms on other edges. The vector for the site is defined as pointing from the center of mass of these four atoms to the site point.

- Bridge sites:

  - Edge:

    * Outer (fig. 3.3g): The point is defined as the center of mass of a vertex atom and one of the neighbouring edge atoms. The vector is found by taking the vector from the center of mass of the whole cluster to the site point, and then subtracting the projection of this onto a vector between the chosen vertex and edge atom.

    * Inner (fig. 3.3h): Like the above, but using two edge atoms along the same edge instead.

  - Face:

    * Inner (fig. 3.3j): A bridge site between a face atom and a neighbouring edge atom, the center of mass of these two are defined as the site point. To find the vector, notice that these two atoms form a rhombus on the face of the cluster with two other neighbouring atoms. The site vector is defined as a unit vector pointing away from the cluster parallel to the cross product of the vectors between opposite vertices of this rhombus.

    * Outer (fig. 3.3i): A bridge site between an edge atom and another edge atom on a different edge. Defined as the above, but with the last two vertices of the rhombus given by the neighbouring vertex and face atoms.

66

- Hollow sites:

  - Face (fig. 3.3d): The site point is the center of mass of three atoms, one face atom and two neighbouring edge atoms which are themselves neighbours of the same vertex atom. The site vector is the normal vector to a plane defined by two vectors, each of them pointing from the face atom to one of the edge atoms.

  - Vertex (fig. 3.3e): Like the above, but with the three atoms being a vertex atom and two neighbouring edge atoms on the same face.

  - Edge (fig. 3.3f): Like the above, but with the three atoms being one face atom and two edge atoms along the same edge.